scientific reports

Check for updates

OPEN

Multidisciplinary high resolution Geophysical Imaging of Pantano Ripa Rossa Segment of the Irpinia Fault (Southern Italy)

Pier Paolo G. Bruno[1,2], Giuseppe Ferrara[1✉], Miller Zambrano[3], Stefano Maraio[4], Luigi Improta[5], Tiziano Volatili[3], Vincenzo Di Fiore[6], Giovanni Florio[1], David Iacopini[1], Filippo Accomando[1], Daniela Tarallo[6], Paolo Marco De Martini[4], Filippo Muccini[2], Michele Punzo[6], Valeria Paoletti[1,8], Stefano Albanese[1], Antonio Iannone[1], Lucia Rita Pacifico[1], Annamaria Vicari[7], Nicola Angelo Famiglietti[7], Antonino Memmolo[7], Giuseppe Cavuoto[6] & Maurizio Milano[1]

The Irpinia Fault, also known as the Monte Marzano Fault System, located in the Southern Apennines (Italy), is one of the most seismically active structures in the Mediterranean. It is the source of the 1980, Ms 6.9, multi-segment rupture earthquake that caused significant damage and nearly 3,000 casualties. Paleoseismological surveys indicate that this structure has generated at least four Mw ~ 7 surface-rupturing earthquakes in the past 2 ka. This paper presents a comprehensive, high-resolution geophysical investigation focused on the southernmost fault segment of the Monte Marzano Fault System, i.e., the Pantano-Ripa Rossa Fault, outcropping within the Pantano di San Gregorio Magno intramontane basin. The project, named TEst Site IRpinia fAult (TESIRA), was supported by the University of Napoli Federico II to study the near-surface structure of this intra-basin fault splay that repeatedly ruptured co-seismically in the past thousands of years. Our imaging approach included 2D and 3D electrical and seismic surveys, gravimetry, 3D FullWaver electrical tomography, drone-borne GPR and magnetic surveys, and CO_2 soil flux assessment across the surface rupture. This multidisciplinary investigation improved our understanding of the basin shallow structure, providing an image of a rather complex subsurface fault and basin geometry. Seismic data suggest that fault activity at the Pantano segment of MMFS is characterized by a near-surface cumulative displacement greater than previous estimations, calling into question earlier assumptions about the timing of its activation. Despite some challenges with our drone-mounted survey equipment, the integrated dataset provides a comprehensive and reliable image of the subsurface structure. This work demonstrates the utility of developing an integrated approach at high-resolution geophysical imaging and interpretation of fault zones with weak morphological expressions.

The Southern Apennines range is among the areas with the highest seismogenic potential in the Mediterranean region. This is for instance the case of the so-called Irpinia Fault (i.e., Monte Marzano Fault System or MMFS), the source of the third largest Italian earthquake of the last century (1980, Ms 6.9, Irpinia earthquake[1,2]). The 1980 Irpinia Earthquake was a normal faulting event characterized by multiple ruptures along different segments, highlighting the complexity of the MMFS. In fact, the epicentral locations and source models have been debated by many authors[3–7]. The MMFS was only recognized after the 1980 earthquake, through the study of coseismic scarps[2,8,9] and timing of paleo-earthquakes, on various fault segments activated during the 1980

[1]Dipartimento di Scienze della Terra, dell'Ambiente e delle Risorse, Università degli Studi di Napoli "Federico II", Napoli, Italy. [2]Sezione di Geomagnetismo, Aeronomia, e Geofisica Ambientale, Istituto Nazionale di Geofisica e Vulcanologia, Roma, Italy. [3]Scuola di Scienze e Tecnologie - Sezione di Geologia, Università di Camerino, Camerino, Italy. [4]Sezione Sismologia e Tettonofisica, Istituto Nazionale di Geofisica e Vulcanologia, Roma, Italy. [5]Osservatorio Nazionale Terremoti, Istituto Nazionale di Geofisica e Vulcanologia, Roma, Italy. [6]Istituto di Scienze e Patrimonio Culturale (ISPC-CNR), Napoli, Italy. [7]Sezione Irpinia, Istituto Nazionale di Geofisica e Vulcanologia, Grottaminarda, AV, Italy. [8]Sezione Osservatorio Vesuviano, Istituto Nazionale di Geofisica e Vulcanologia, Napoli, Italy. ✉email: giuseppe.ferrrara@unina.it

event[3]. These studies revealed that the Irpinia Fault represents a major seismogenic source in the Southern Apennines, despite its subtle geomorphic expression. This subtlety is attributed mainly to the fault's relatively recent inception, estimated by different authors to have occurred between the Middle and Upper Pleistocene, based on geomorphic and radiometric evidence[1,2,10].

The largest (M6+) earthquakes of the central and southern Apennines result from the multi-segment rupture of normal fault systems striking NW-SE along the axial zone of the range. Regardless of their seismogenic potential, these fault systems may either exhibit clear geomorphic expressions, typically bounding large and deep intermountain basins, or they may be weakly expressed at surface by short-term geomorphological indicators, such as small fault scarps, counter slope scarps and dammed valleys with associated small basin.

In the first case, the subsurface fault architecture, and the geometry and evolution of hangingwall basins can be effectively analyzed by reinterpreting commercial seismic profiling. A good example is the large Fucino basin, bounded by the causative fault of the 1915, Mw 7 Marsica earthquake[11,12], which is filled by a > 1000 m thick continental succession[13]. For the latter type of fault systems, such as the Irpinia Fault, the associated hangingwall basins are often too small to be adequately imaged by conventional seismic profiles. High-resolution, multidisciplinary geophysical investigations are required to better characterize their subsurface structures (see Improta et al[14]. and references therein).

Recent efforts have been made to relate the surface rupture of the Irpinia earthquake to deep structures interpreted from vintage, poor-quality seismic data[15]. However, even after reprocessing, these data often lack the resolution needed to accurately characterize the shallow features. Interpretation based on such data[17] could be significantly refined with new, high-resolution geophysical data[15,17]. Moreover, a deeper understanding of the shallow structure of young seismogenic faults and their interaction with basin evolution and sedimentation processes, important for seismic hazard assessment, requires integrating three-dimensional and multivariate subsurface imaging techniques. The TEst Site IRpinia fAult (TESIRA) project provided a unique opportunity to collect 3D geophysical data with unprecedented detail across the southern segment of the Irpinia Fault, the Pantano-Ripa-Rossa Fault[18–20]. Previous shallow seismic profiles have demonstrated that this fault, along with its associated basin, i.e., Pantano di San Gregorio Magno (Fig. 1B) has a geometric complexity that cannot be fully captured by 2D surveys.

The site logistics of Pantano di San Gregorio Magno were ideal for testing the integration of different geophysical imaging technologies and allowed us to conduct the first 3D high-resolution pilot study across a representative outcrop of an active fault in mainland Italy. 3D high-resolution seismic imaging, typically used in oil exploration, marks a significant advance in understanding the near-surface structure and kinematics of seismogenic faults. The acquired data included seismic and electric surveys, gravity measurements, CO_2 soil degassing measurements, and drone-borne ground-penetrating radar or GPR and magnetic surveys. These efforts aim to foster the development and testing of joint processing and interpretation techniques customized for imaging of active faults, enhancing our ability to detect active fault strands and providing a robust analog for similar seismically active environments.

In this paper, we discuss the planning and execution of all surveys and evaluate the data quality and performance of each method. Specifically, the 3D seismic acquisition was conducted using equipment primarily designed for 2D surveys; we go into the details of the field techniques used to enable others to replicate our experiment. Overall, the acquired data were of high quality and highly informative. In particular, the electric FullWaver and gravity data allowed us to estimate the geometry and extent of this small intramontane basin associated with active faulting, offering new insights into the interaction between surface faulting and basin development in this key area of the Southern Apennines.

## Geology of Pantano di San Gregorio Magno

Pantano (i.e., swamp) di San Gregorio Magno (hereinafter referred to as Pantano: Fig. 1) is a Quaternary, intermontane tectono-karstic depression centrally located within the Southern Apennines and developed into Mesozoic limestones. The basin is filled by late Middle Pleistocene - Holocene lacustrine deposits (clays, sands and silts) with intercalation of tephra layers and sandy levels rich in reworked volcanic material[21]. The lacustrine sediments pass laterally and/or are covered by Late Pleistocene - Holocene alluvial fan and slope carbonate deposits which crop out along the basin edges[21,22] (Fig. 1). The basin opening and evolution was mainly controlled, since the Middle Pleistocene, by WNW-ESE trending range-bounding normal faults (i.e. Pantano - S. Gregorio Magno, PSGM Fault System[21,22]) related to the NE-trending regional extension. Thanks to tephra layers interbedded in the lacustrine sediments of a 60-m-deep borehole in the center of the basin[21] (C well in Fig. 1B), Munno and Petrosino[23] determined that sedimentation in the basin began prior to 170 ka (tephra sample S5, at 50.8 m depth, Aiello et al[21].), continuing after the Neapolitan Yellow Tuff eruption of Campi Flegrei (tephra sample S21, at 4.8 m depth, Aiello et al[21].), which took place 14.5 ± 0.4 ka[24].

The Southern Apennines are known for their frequent seismic activity[25–27]. The NE-trending regional extension is presently active, as documented by Montone and Mariucci[28] and previously by Hippolyte et al[29]. and Caiazzo et al[30]. Several destructive historical earthquakes[31] (I_0 > X MCS, Mercalli-Cancani-Sieberg Macroseismic scale[32]) struck this sector of the Apennines (Fig. 1). The 1980, Ms 6.9 Irpinia earthquake occurred on November 23rd, caused by the rupture of three main normal fault segments that strike 310–320° and dip 60–70° NE[2,4,5]. These three main strands, separated by two gaps, formed an overall 38-km-long system[33,34] and were associated with surface ruptures and coseismic scarps up to 1.3 m high[1]. The Pantano scarp (Figs. 1 and 2) belongs to the southernmost Irpinia fault strand, the Pantano-Ripa-Rossa Fault[2,6]. This co-seismic scarp, running in the eastern sector of the basin, was 45–50 cm high[35]. After 44 years, agricultural modifications have almost completely obliterated the scarp that is instead well-preserved along the Ripa Rossa ridge[15] (Fig. 1B).

The in-depth structure of the Pantano basin was investigated in 2006 by three high-resolution seismic profiles which represented a solid guide for our survey design (Fig. 2). The shortest profile was published by Bruno et al[19].
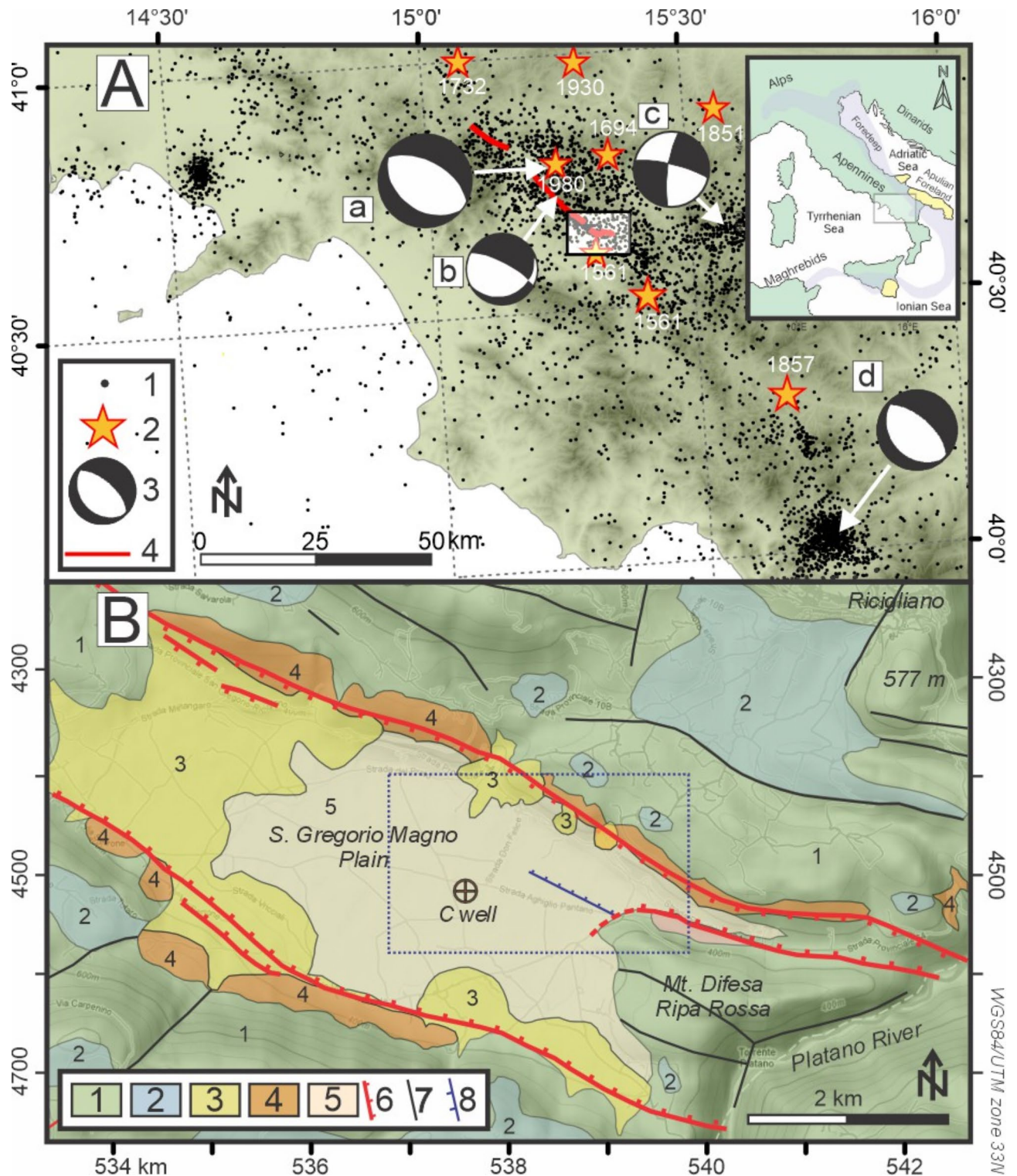
Fig. 1. (A) Seismicity of the Southern Apennines, with the upper right inset revealing the region's location relative to the Italian peninsula. The elements of the upper map include: 1 - Instrumental seismicity[25]; 2 - Historical earthquakes (M > 6); 3[25]- Focal mechanism of M > 5 events[27](a - Irpinia fault 1980 M6.9; b - Irpinia fault 1996 M5.1; c - Potenza seismic sequence 1990 M5.7; d - Mercure earthquake sequence 1998 M5.6); 4 - Fault scarps from the 1980 Irpinia earthquake[10,21]. The transparent box outlines the area in Fig. 1B. (B) Geological map of the Pantano basin. (modified from Aiello et al[21].) showing: 1 - Mesozoic limestones, 2 - Middle Pliocene sands and conglomerates, 3 - Alluvial fan deposits (Middle Pleistocene-Holocene), 4 - Slope debris (Middle Pleistocene- Holocene), 5 - Lacustrine and colluvial deposits (Upper Pleistocene- Holocene), 6 - Quaternary normal faults (PSGM Fault System), 7 - High-angle faults, 8–1980 Earthquake surface scarp. The dotted rectangle outlines the location of Fig. 2 in relation to the Pantano Basin. This figure was generated with Corel Draw 24.
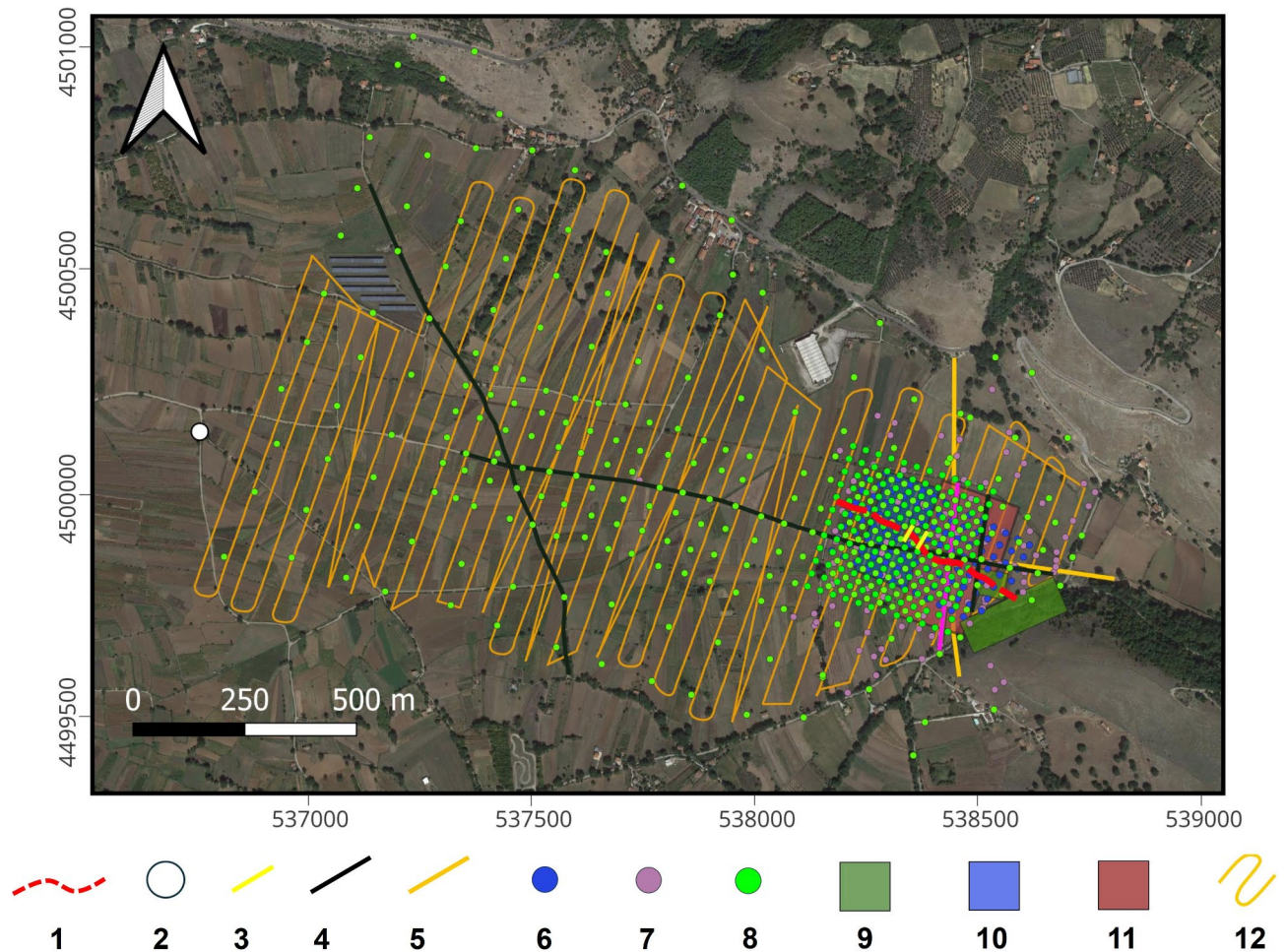
Fig. 2. Satellite image from Google Earth Pro, v. 7.3.3 (https://www.google.com/earth/) illustrates the extent of field surveys conducted in the Pantano San Gregorio Magno basin, showing: 1 - the 1980 Irpinia Earthquake scarp, 2 - the location of Core C well (Aiello et al[21].), 3 - the positions of paleoseismological trenches[36], 4 - the black lines indicate the 2D seismic profiles acquired in 2006 while the magenta line indicate Pantano_4, acquired in July 2022, 5 - the Electrical Resistivity Tomography profiles location, 6 - the CO_2 flux measurement stations, 7 - FullWaver measurement points (Rx and Tx stations), 8 - Gravity field measurement stations, 9 - Ground-Penetrating Radar acquisition area, 10 - the area covered by the 3D electric survey, 11 - the area surveyed with 3D seismic method, 12 - the flight paths of drone-borne magnetometric surveys.

They recorded dense buffalo-gun shots with 1.5-m-spaced geophones deployed across the 1980 scarp to obtain a shallow, very-high resolution image of the intra-basin fault-zone. The obtained Pre-Stack Depth Migration section, co-located with a previous paleoseismic trench[36], showed that in the downthrown side, faulting activity has led to the formation of colluvial bodies and to the thickening of lacustrine deposits. Seismic data showed the tilting and growth of the shallow lacustrine strata towards the fault caused by its sin-sedimentary activity. By combining the 29–38 m vertical slip of the fault, inferred from their seismic section with a vertical slip rate of 0.3 mm/yr estimated by trench data[3], Bruno et al[19]. tentatively estimate an age of 97–127 ka for the inception of the fault, during the Middle-Upper Pleistocene period. The map was generated by QGIS v. 3.28 Firenze (https://qgis.org/).

Methods

The Pantano basin formation exceeds 240 ka, being probably around 300 ka[10]. As discussed above, the accommodation space created by active faulting has been filled with coarse sediments derived from the weathering of surrounding carbonate reliefs and by fine lacustrine sediments[21]. Overlap and contact of sediments/rocks with different seismic velocities, densities and resistivities make the basin and the associated fault zone well suitable for investigation using geophysical methods. In theory, our multi-parametric, multi-scale geophysical survey at Pantano positions the GPR survey as the highest in resolution (centimeter scale) but with very shallow penetration. On the opposite end, potential methods like gravity and magnetic surveys offer lower resolution (several tens of meters) but greater penetration, while seismic data falls in between, providing metric resolution. The magnetic and GPR data were acquired using an "Unmanned Aerial Vehicle" (UAV), i.e., a drone. The use of drones leads to cost reduction, time savings, and decreased risks if compared to the common ground

and airborne surveys and allows dense and uniform aerial coverage. Additionally, UAV surveys, in the case of difficult ground conditions, may represent the only alternative for data acquisition[37].

Active seismic surveys

The seismic data were collected in July 2022 and include a high-resolution 3D seismic survey along with a 2D profile. The surveyed region was well-suited for on-land seismic acquisitions owing to minimal topographical variations. However, logistical challenges arose, primarily related to land accessibility issues, including the presence of crops during the experiment. Especially for the 3D experiment, securing permits from numerous landowners proved challenging, preventing the realization of the initially planned survey volume. Both datasets intersect the 1980 scarp of the Irpinia Earthquake, as illustrated in Fig. 2. The source was a high-resolution seismic vibrator, the IVI-MiniVib, identical to the one used to acquire the three high-quality seismic profiles (see location in Fig. 2) in 2006. At each vibration point this source released approximately 27 kN of energy, distributed over a 15-second window and across a linear frequency range of 5–200 Hz. The data were recorded by vertical geophones with a 4.5 Hz eigen-frequency at a sampling rate of 1 ms and for a record length of 16 s. A/D conversion was carried out using the Geometrics distributed Geode acquisition systems, featuring 24-bit technology.

2D seismic. The only seismic profile acquired during the project, Pantano_4 (Fig. 2), complements the three profiles recorded in 2006. The profile Pantano_4 cuts across the 3D volume perpendicular to the surface rupture of the 1980 Irpinia Earthquake and is nearly parallel to the very-high resolution profile published by Bruno et al[19]. that involved buffalo-gun shots. To achieve high-resolution imaging, a small spatial sampling interval was used: specifically, a receiver spacing of 2 m and a source spacing of 4 m. The 99 vibration points moved from southwest to northeast along a 190-receiver line (8 Geodes) covering a length of 377.5 m. The maximum fold achieved is 99, resulting in a total of 18,810 traces, with an elevation gap along the profile of only 5.6 m.

3D seismic. The location and geometry of the source and receiver array we have designed for the 3D acquisition are shown in Fig. 3 and Supplementary Fig. 1. We have chosen a non-orthogonal acquisition geometry[38], with an angle of 45° between receiver and source lines. This configuration effectively mitigates the evident acquisition footprints observed at shallow levels in layouts where source and receiver lines are arranged orthogonally. The recording array comprises seventeen receiver lines oriented at N-7°E, each equipped with 48 vertical geophones at 4.5 Hz, totaling 816 geophone nodes connected to a Geode acquisition system. Additionally, there are 41 source lines oriented approximately N-62°E, featuring a variable number of vibration points ranging from 1 to 40, resulting in a total of 784 acquired vibration points. The collective surface coverage spans approximately 12.5 acres or 50,468 m².

The Geode acquisition system is primarily designed for 2D profiles. Consequently, we had to modify the system to accommodate a 3D acquisition, which involves a significantly larger number of channels. The Geode system digitizes the data locally, with each board handling the digitization of 24 channels. The data from these channels are then transmitted to the acquisition PCs through an Ethernet cable that connects all the boards in a cascade to a single PC. Due to the large number of channels required for 3D acquisition, data transmission can be time-consuming. To address this, we divided the acquisition array into four separate sub-arrays, with each pair of sub-arrays connected to a different Ethernet card in the acquisition PC, as depicted in Supplementary Fig. 1. Merging the data, remapping seismic channels, and editing traces (such as removing dead traces and identifying reversed ones) was particularly challenging due to the large number of waveforms involved. Supplementary Fig. 2 displays the traces acquired at Vibration point #275 (refer to the map in Fig. 3) by the four sub-arrays, after trace editing and channel remapping. The survey location and parameters were selected with the goal to capture signals from depths of a few meters up to about 350 m, covering the entire basin depth. A maximum offset of 350 m was used to image near-surface velocity features across the 1980 surface rupture using 3D first arrival tomography.

We organized the data into common midpoints (CMP) with a square bin size of 25 m² (5×5), yielding an inline fold of 6 and a crossline fold of 9, resulting in a total fold of 54[39]. Seismic reflection processing aimed at obtaining a depth-migrated seismic volume using traditional CMP processing with post-stack depth migration algorithms[40]. The process began with channel remapping due to the complex array configuration, followed by 3D geometrization. The workflow included steps to eliminate noise, reduce artifacts, and enhance resolution[40].

The initial step involved trace editing to remove noisy or dead traces, mainly caused by poor ground coupling and loose electric contacts, and to correct polarity reversals[41]. Data correction included amplitude normalization to balance wave attenuation and bandpass filtering to reduce noise[42,43]. Minimum phase conversion of the seismic wavelet was achieved by estimating an inverse filter from the source sweeps. Deconvolution was applied to remove the source wavelet effects from the data and to predict and attenuate reverberations and multiples[41,44,45]. Subsequent processing included static correction to align all traces to a common reference level (datum: Hileman et al[46]) and velocity analysis[47–49], which was essential for applying Normal Moveout (NMO) correction to account for travel-time differences between the source and receivers. Data reduction and enhancement were carried out through common midpoint stacking, where traces in each CMP gather were summed after NMO correction, enhancing primary reflections while reducing noise and multiples. The final step was relocating seismic reflectors to true subsurface positions through depth migration[50].

Figure 4 presents a combined view of inline 20, crossline 25, an oblique random line, and a horizontal slice at a depth of 125 m from the post-stack depth-migrated 3D seismic data gathered at Pantano. This image highlights the near-surface features of the Pantano-Ripa-Rossa Fault and illustrates its relationship with the surface rupture from the 1980 Irpinia earthquake. In Supplementary Fig. 3, we compare the oblique random line with the 2D profile Pantano_3 presented by Bruno et al[19]. For the latter profile, the CMP spacing is only 0.75 m, whereas in the oblique slice, it is 2.5 m. Additionally, truck noise from the MiniVIB source limits the imaging of reflectors shallower than ~25 m in the 3D volume. However, the higher source power of the MiniVIB provides a better
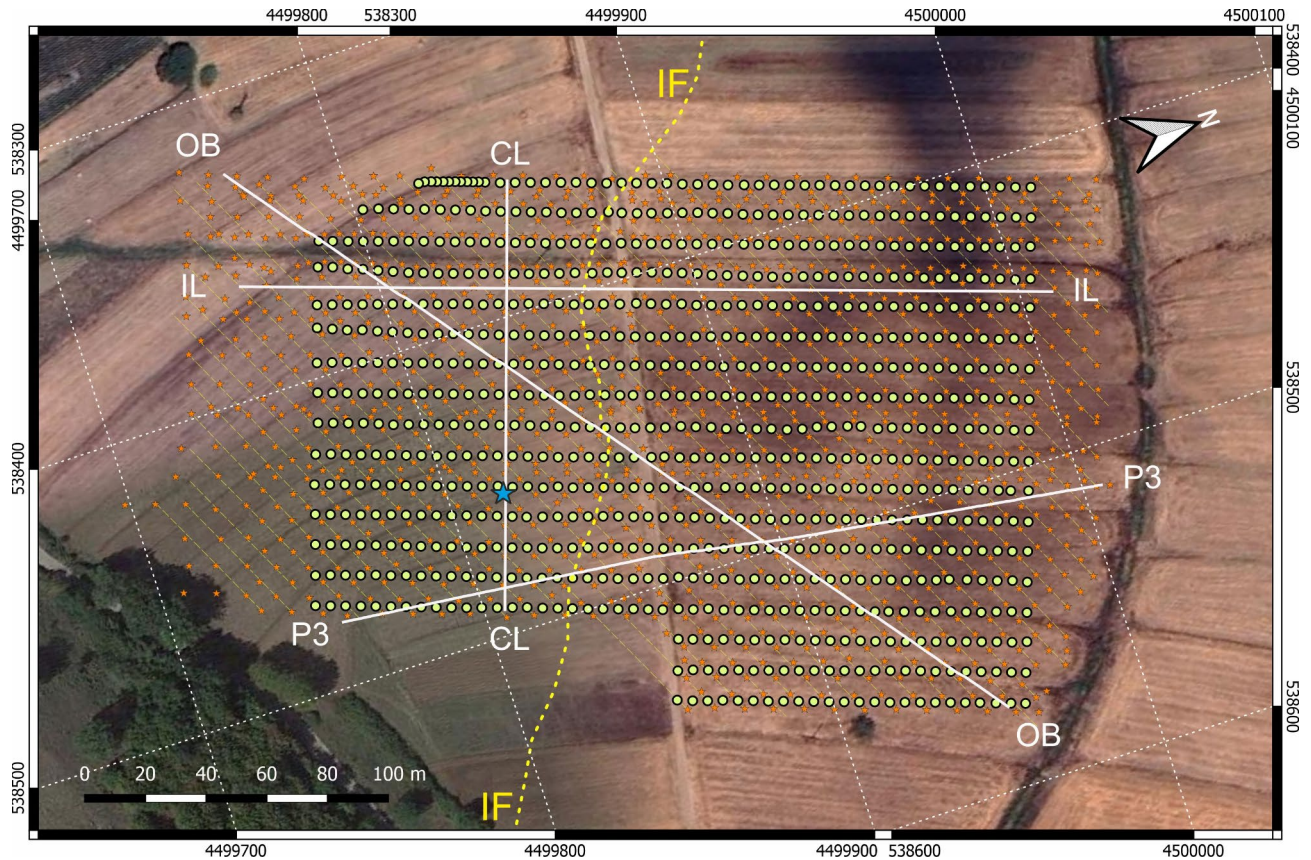
Fig. 3. Satellite image from Google Earth Pro, v. 7.3.3 (https://www.google.com/earth/), illustrates a detailed view of the 3D seismic acquisition geometry, with receiver lines (green dots) and source lines (red stars). The inline receiver spacing is 5 m, with receiver lines positioned 15 m apart. The map was generated by QGIS v. 3.28 Firenze (https://qgis.org/).Source lines are spaced approximately 7.5 m both in the inline and crossline directions. The angle between receiver and source lines is ~ 45°, and irregularities in source points are due to logistical constraints. To investigate areas with insufficient coverage or a low signal-to-noise ratio in the acquired data, additional vibration points were randomly added at the end of the survey. The blue star shows the position of vibration point #275 whose common shot gather is shown in Supplementary Fig. 2. The three white segments correspond to the seismic profiles shown in Figs. 4 and 5. Symbols: IL - Inline profile # 20; CL - Crossline profile # 25; OB – Oblique profile; P3–2D very-high resolution profile Pantano_3 published by Bruno et al[19].

signal-to-noise ratio and greater depth penetration. The interpretation of Supplementary Fig. 3 is shown in Fig. 5 and will be discussed in detail in the next section. Even at this preliminary stage, the results in Figs. 4 and 5 offer a clear view of the complex geometry of the basin, revealing the subsurface pattern of the carbonate basement and basin stratigraphy.

2D and 3D electric data

Electrical resistivity tomography (ERT) is a geophysical technique used to map the spatial distribution and contrasts of electrical resistivity in the subsurface, producing high-resolution 2D/3D images of underground structures[51–53]. ERT is effective for reconstructing buried lithologies, inferring hydrogeological characteristics, and identifying active faults, often in conjunction with seismic methods[14,54–60]. It works by measuring the potential difference caused by a known current to calculate apparent resistivity and chargeability[61]. In our 3D acquisition, electrode profiles were aligned with the N 7°E strike of the geophone lines, though the grid only partially overlaps with the seismic grid due to logistical constraints (Fig. 2 and Supplementary Fig. 4).

The 3D survey area spans 57,500 m² and was organized along a 9-profile rectangular grid, each with 24 stainless steel electrodes spaced 10 m apart and 30 m between lines, totaling 216 electrodes (Fig. 2 and Supplementary Figs. 4–5). Each profile is 230 m long. The 2D electric profiles ERT1 and ERT2, which overlap with seismic profiles Pantano_2 and Pantano_4, used 60 and 72 channels, respectively, with 10 m electrode spacing. Data were collected with an IRIS Syscal PRO 96 resistivity meter equipped with a 120-channel switch. The resistivity meter can automatically perform a predefined set of measurements, and provides a direct reading of input current, potential difference, electrode location and apparent resistivity (see Supplementary Fig. 6).

For the 3D acquisition, given the relatively small data coverage, we employed a Dipole-Dipole array and a cross-diagonal survey to optimize measurement efficiency and reduce survey time, following the approach
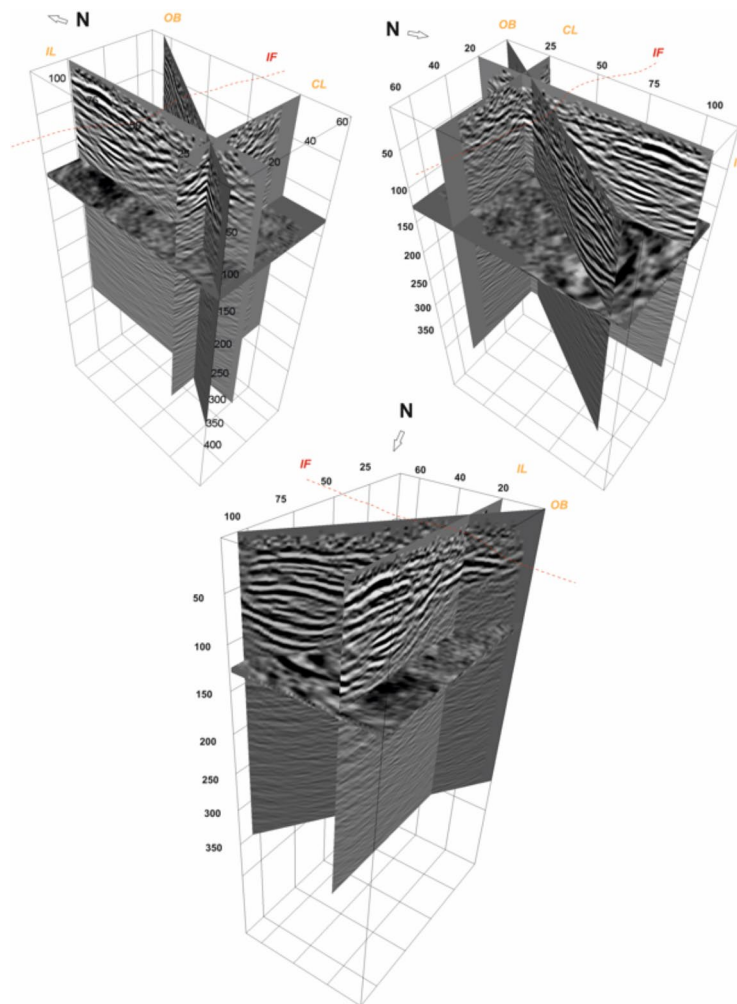
Fig. 4. Unified 3D view of inline (IL) # 20, crossline (CL) # 25 (only upper images), an oblique random line (OB) and a horizontal slice cut at a depth of 125 m of the post stack depth-migrated 3D seismic dataset from three different perspectives. The position of the slices is shown in Fig. 3. IF is the trace of the surface rupture which occurred during the 1980 Irpinia earthquake. This figure was generated with Corel Draw 24.

outlined by Loke and Barker[62]. This setup enabled rapid and effective measurement of electric potential along the profiles (x-axis), across profiles (y-axis), and along 45° diagonal lines.

The quality of the apparent resistivity data was affected by electrical power cables underground, leading to the exclusion of approximately 14% of the data before inversion. The theoretical depth of investigation[63] reaches 55 m. We inverted the apparent resistivity data using the algorithm by Loke and Barker[62]. Initially, a conventional least squares method minimized the squared differences (L2 norm) between measured and calculated values. Subsequently, a robust model constraint was applied to minimize the absolute differences (L1 norm), which reduces the impact of noisy data points. Figure 6 displays the resistivity distribution with depth from the inverted 3D volume in the x-z plane. The shallow depth slices show significant lateral resistivity variations, while deeper slices exhibit reduced resolution. The inverted resistivity values range from 5 Ωm to 20 Ωm.

3D deep electric resistivity tomography (FullWaver)

The deep geoelectrical survey used 15 wireless dual-channel digital receivers (V-FullWaver, IRIS Instruments) to record signals from a 5-kW time-domain induced polarization transmitter (VIP-5000) with multiple current injections. The FullWaver stations enabled accurate time-domain measurements of induced polarization, resistivity, and self-potential, overcoming traditional limitations of array configurations and topography. This method is similar to the quadrupole measurement principle used in multi-electrode resistivity profiling systems[64–66], where current is injected into the ground through two electrodes (AB) and the resulting voltage is measured by two other electrodes (MN). Real-time recording of input current is performed by independent stations, each with its own power source, GPS module, and digital memory for continuous recording. Synchronization of devices is achieved through a GPS PPS signal, providing precise time stamping with an accuracy of 250 µs.
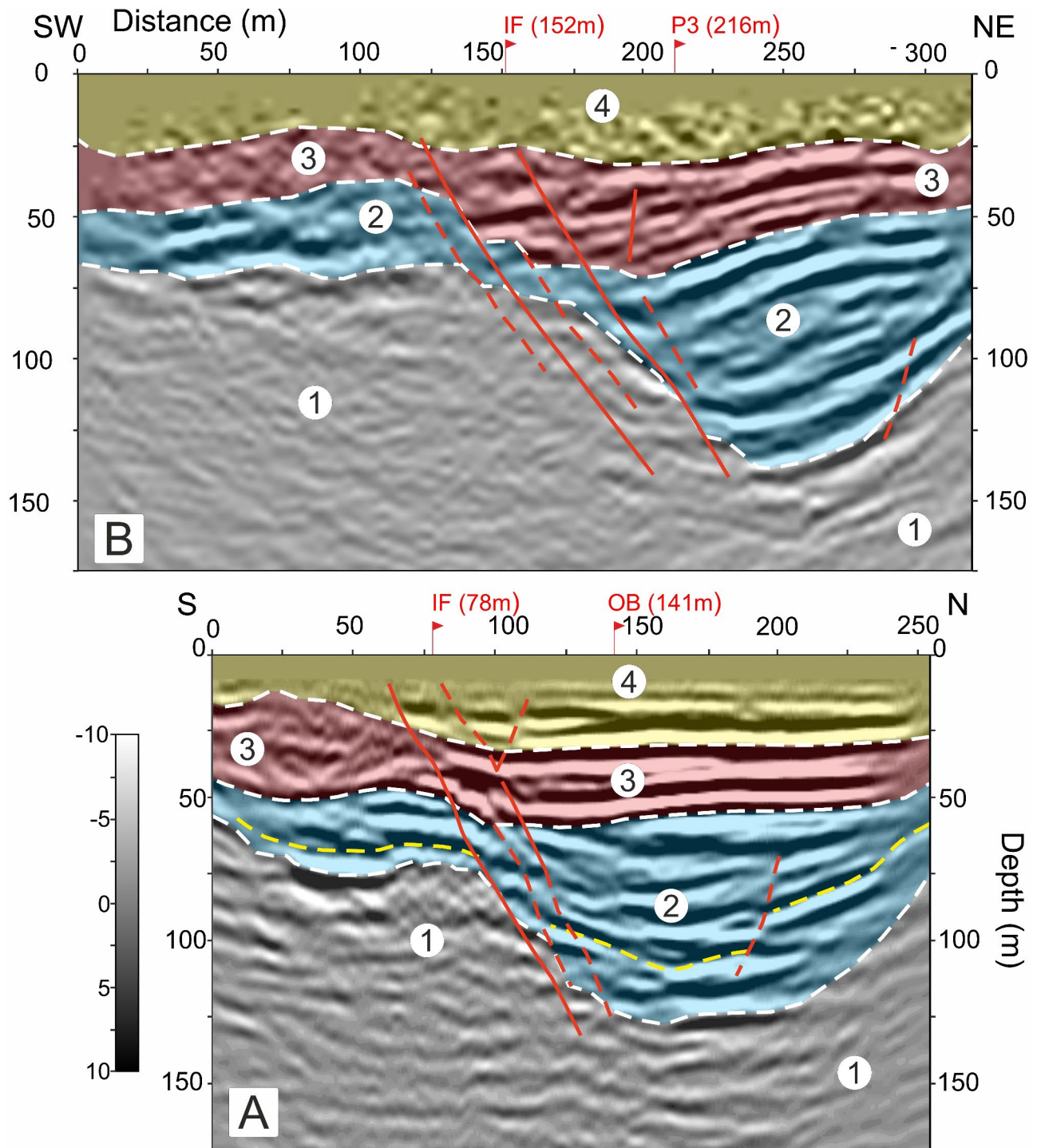
Fig. 5. Reinterpretation of seismic profile Pantano_3 (A) published by Bruno et al[19]. compared with the interpretation of random line (B) extracted from the seismic volume (Fig. 4). Line locations are in Fig. 3. Symbols: 1 - Mesozoic carbonates (transparent), 2 - Upper Pleistocene - Holocene dense/cemented carbonate slope debris (transparent) alternating to tilted lacustrine deposits and alluvial fans, 3 - Upper Pleistocene - Holocene highly reflective lacustrine (in the fault hanging-wall) and poor reflective coarser deposits (in the fault foot-wall), 4 - Holocene lacustrine and slope deposits, and colluvium. IF - 1980 Irpinia Earthquake surface rupture. Fault splays are highlighted by red lines (dashed: hypothetical). The yellow dashed line outlines the position of the top of the basement according to the interpretation of Bruno et al[19]. which has been revised.
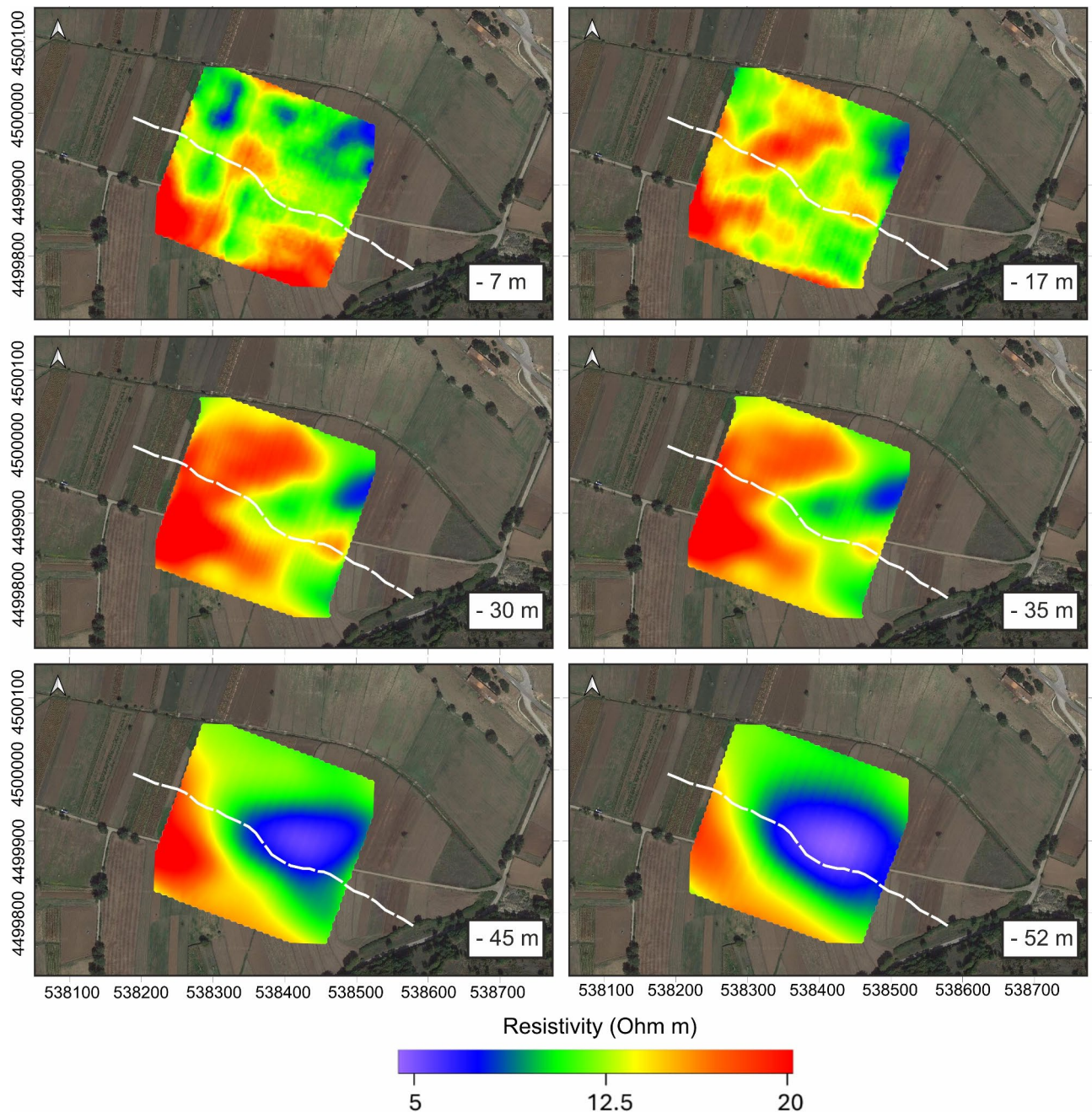
Fig. 6. Horizontal slices cut from 3D resistivity cube model of across six different depth intervals displayed on satellite image from Google Earth Pro, v. 7.3.3 (https://www.google.com/earth/). The dashed white segment is the coseismic surface rupture that occurred during the 1980 Irpinia Earthquake.

The survey aimed to achieve a depth of at least 150 m, covering the area where surface fault rupture was reported (Fig. 7). By using current dipoles (AB) with apertures up to 1000 m, theoretical depths of around 200 m were reached. The survey was conducted over two days to gather sufficient data and achieve the desired resolution within the area previously explored with 3D seismic methods. During the survey, 90 electrodes (receivers) and 24 current input locations (transmitters) were used. Receivers with variable apertures (25–50 m) and dipole orientations (E-W and N-S) facilitated different quadrupole configurations. Current injections ranged from 2 to 3 A, adjusted based on TX dipole sizes and ground resistance (the higher the TX size and the ground resistance the lower was the injected current). Polarity reversals every 2s during current transmission minimized electrode polarization effects. The acquisition window lasted about 300 s, allowing for multiple measurements to improve the signal-to-noise ratio.

The transmission and receiver records are synchronized and combined using FullWaver Viewer software (IRIS Instruments) with GPS time stamps from each station (see Supplementary Fig. 7). Synchronization
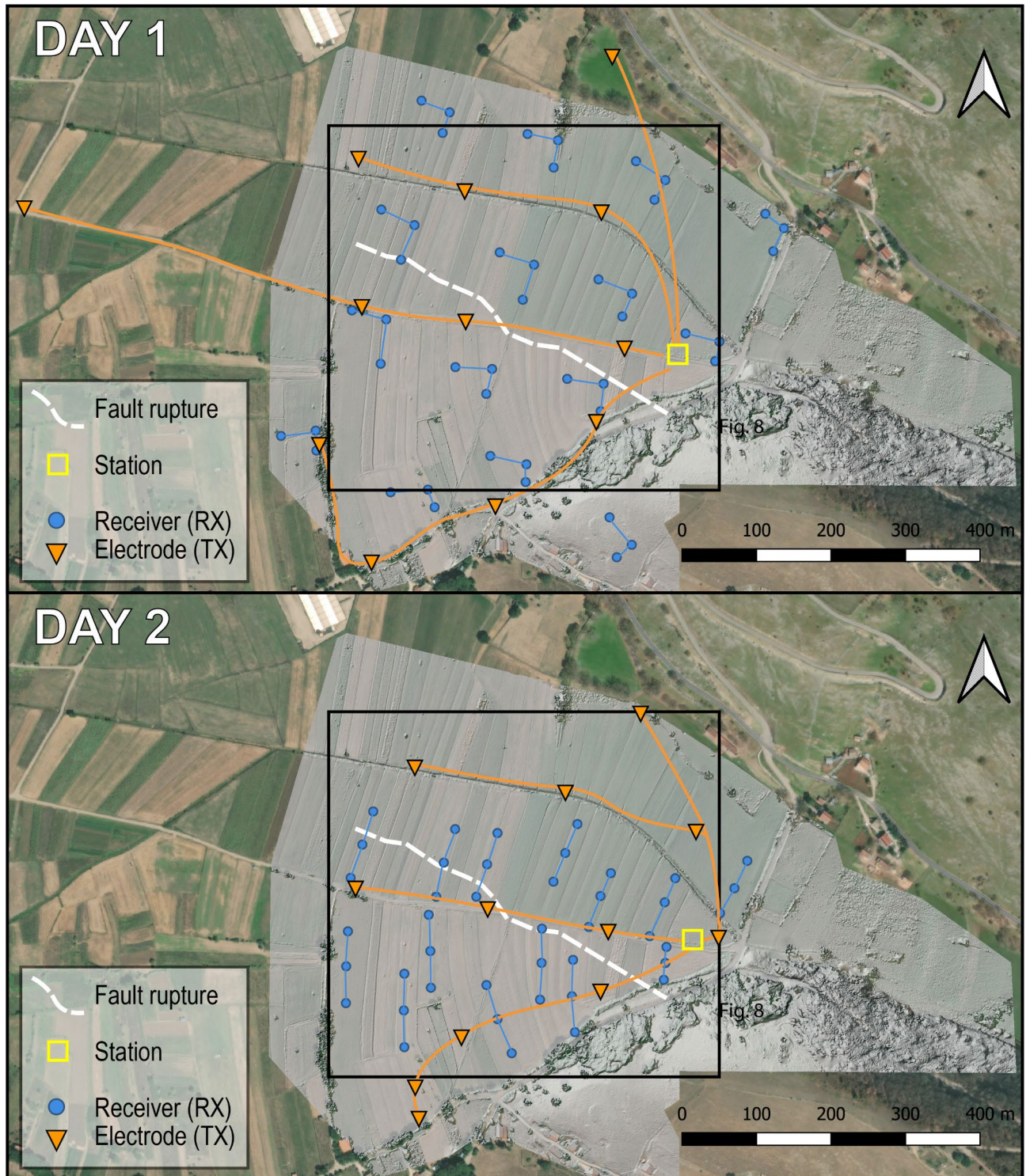
Fig. 7. Satellite image from ESRI World Imagery (https://server.arcgisonline.com/arcgis/rest/services/World _Imagery/MapServer) location of the receivers and transmitters electrodes during the two-day acquisition of the deep geoelectrical survey with the FullWaver system. RX and TX station positions are shown on a high-resolution Digital Terrain Model (DTM) with 0.1 m pixel size obtained by an aero photogrammetric survey made using a DJI Phantom 4 PRO, combined with ground position measurements of electrodes from a GNSS RTK eSurvey E100. The map was generated by QGIS v. 3.28 Firenze (https://qgis.org/).

involves a batch process following a polarity check of receiver electrodes. The process includes identifying and removing spikes and abrupt variations in self-potential, stacking data, and calculating the average voltage during specific injection intervals within the stacked period. Apparent resistivity values are then computed based on the measured resistance. A total of 1920 quadrupoles were processed to obtain electrical current and apparent resistivity values. Quality control ensured data integrity by removing less than 5% of outliers. Filtering of outliers and anomalous values also occurred after preliminary inversion. Consistent with Sapia et al[67]., negative apparent resistivity values, resulting from specific quadrupole combinations and geometries, were excluded from the inversion.

The processed data were modeled using ViewLab 3D software (see Supplementary Fig. 8) with regularized inversion incorporating smoothness constraints to handle significant subsurface resistivity changes and generate robust 3D resistivity models. A medium-resolution mesh ($12.5 \times 12.5 \times 12.5$ m) was created with a depth of 250 m. Topography was obtained from an aerial survey using a DJI Phantom 4 PRO, combined with ground position measurements from a GNSS RTK eSurvey E100. This produced a high-resolution Digital Terrain Model (DTM) with a 0.1 m pixel size, after filtering vegetation and objects. The theoretical maximum investigation depth (300 m) was estimated, first, by integrating the analytic sensitivity function—for the larger TX/RX combinations—and then by calculating the median z depth, so that the area under the sensitivity curve is equal to 50% of the total area[68]. We parameterized the inversion using a starting model of 500 Ωm based on the expected high resistivity of the carbonate substratum and coarse clastic deposits at the basin edges[67], and assuming that the basin fine-grained infill is mostly covered with survey allowing the model perturbation during the inversion. We imposed an anisotropic roughness scheme $x = 1$, $y = 1$, and $z = 0.1$ to highlight strong resistivity changes expected at the interface between basin infill and the carbonate substratum, without losing the lateral variability expected in the faults affecting the infilling sediments. The estimated data noise was set to 0.5% for V/I measurements. The result is a 3D volume of the distribution of the calculated resistivity that can be sliced and visualized in any direction (Figs. 8, 9 and 10). The electric model tends to be more accurate where most of the stations were located (near the previously reported fault rupture). However, a general trend of resistivity was achieved thanks to the most distant stations.
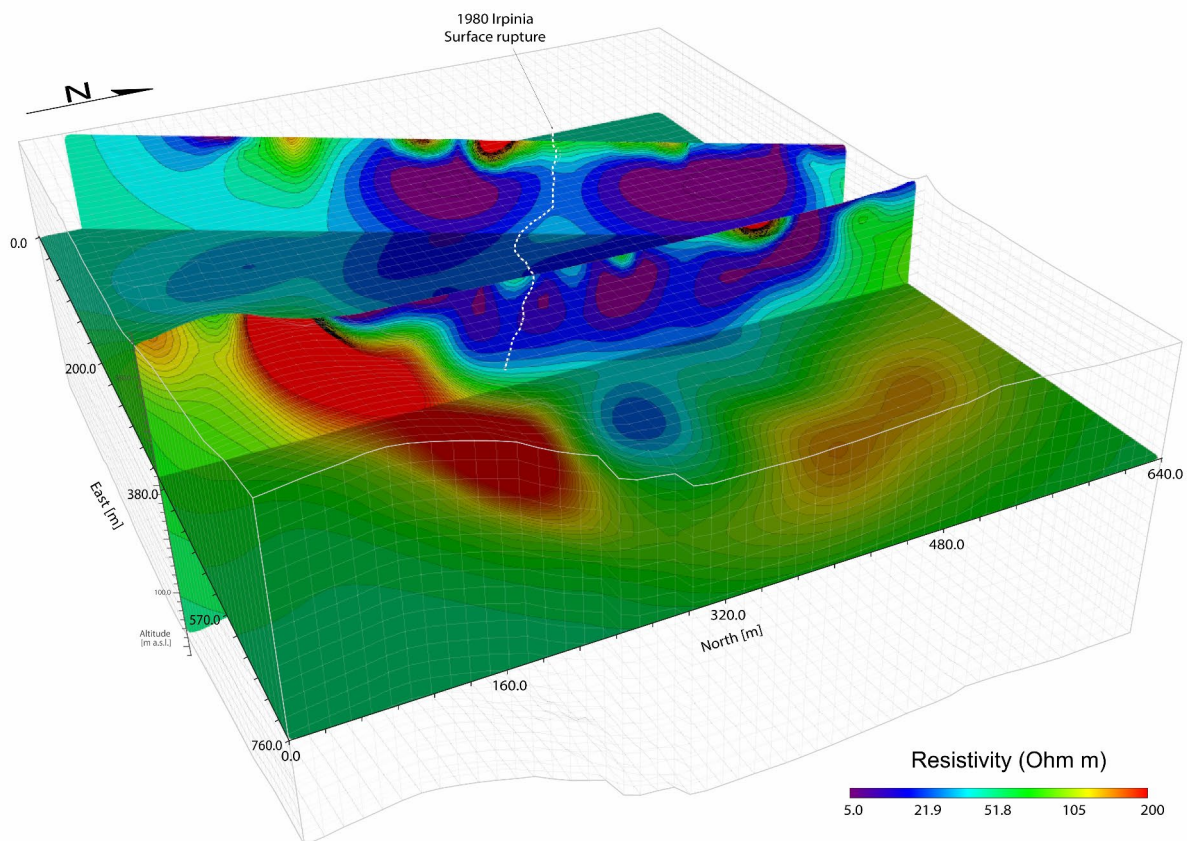
Fig. 8. 3D resistivity model with the projection of the fault rupture in a dashed line on the vertical sections. The Horizontal slice corresponds to the 80 m depth, whereas a N-S section corresponds to $X = 538.450$ m, the diagonal section has a strike of N30E. This figure was generated with ViewLab3D_64 (3.0, http://www.geostud iastier.it).
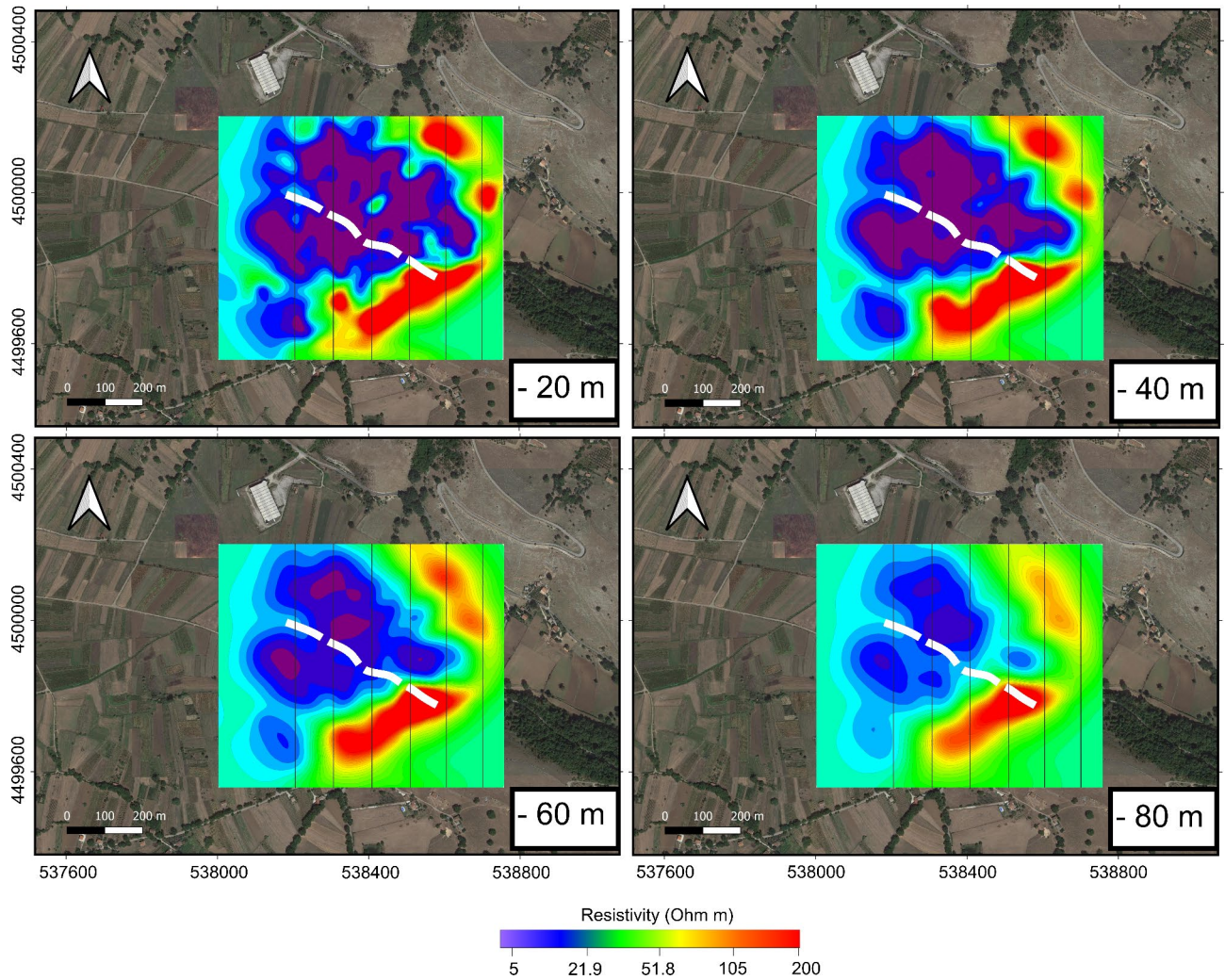
Fig. 9. Horizontal slices cut from 3D resistivity model across four different depth intervals. The dashed white segment is the coseismic surface rupture occurred during the 1980 Irpinia Earthquake, while the black lines correspond to the YZ slice location shown in Fig. 10. This figure was generated with ViewLab3D_64 (3.0, http://www.geostudiastier.it).

Gravity survey

The gravimetric survey involved 442 measurements across a grid covering approximately 1200×1600 m² (Fig. 11). The first survey, conducted in Autumn 2021, included 236 measurements (orange dots in Fig. 11) with 15 m spacing, focusing on the central area of the study, including the Irpinia Earthquake surface rupture. A follow-up survey in September 2023 extended the coverage with an additional 199 measurements spaced 60 to 120 m apart (white dots in Fig. 11).

Measurements were taken using two Autograv Scintrex CG-5 spring-relative gravimeters, each with a 1 µGal resolution and a precision of < 5 µGal. Positioning was achieved with two Stonex high-precision RTK Differential GPS units, offering 1 mm vertical accuracy. The relative offset between the gravimeters was calculated by taking measurements at the same reference point at the beginning and end of the survey. Instrumental drift was monitored by repeated measurements at fixed base stations every hour and 30 min. The raw data were corrected for drift and tide and merged into a single database.

The measured data have been processed using standard procedures based on the Free Air reduction, Bouguer slab reduction and terrain effect correction using the formula[69]:

$$\Delta g_i = g_{obs} - (g_o + g_{fa}) - (g_{bs} + g_t) \tag{1}$$

where Δg_i is the complete Bouguer anomaly, g_{obs} are the observed gravity data, g_o is the theoretical gravity, g_{fa} is the free-air reduction (-0.3086 h, where h is the ellipsoidal elevation at the measuring site), g_{bs} is the Bouguer slab correction and g_t is the terrain effect reduction.

The free-air and Bouguer slab effects were computed using the acquired altimetric data. For the Bouguer slab correction we set a density of ~ 2.6 g/cm³ as representative of the average value of Mesozoic carbonate units
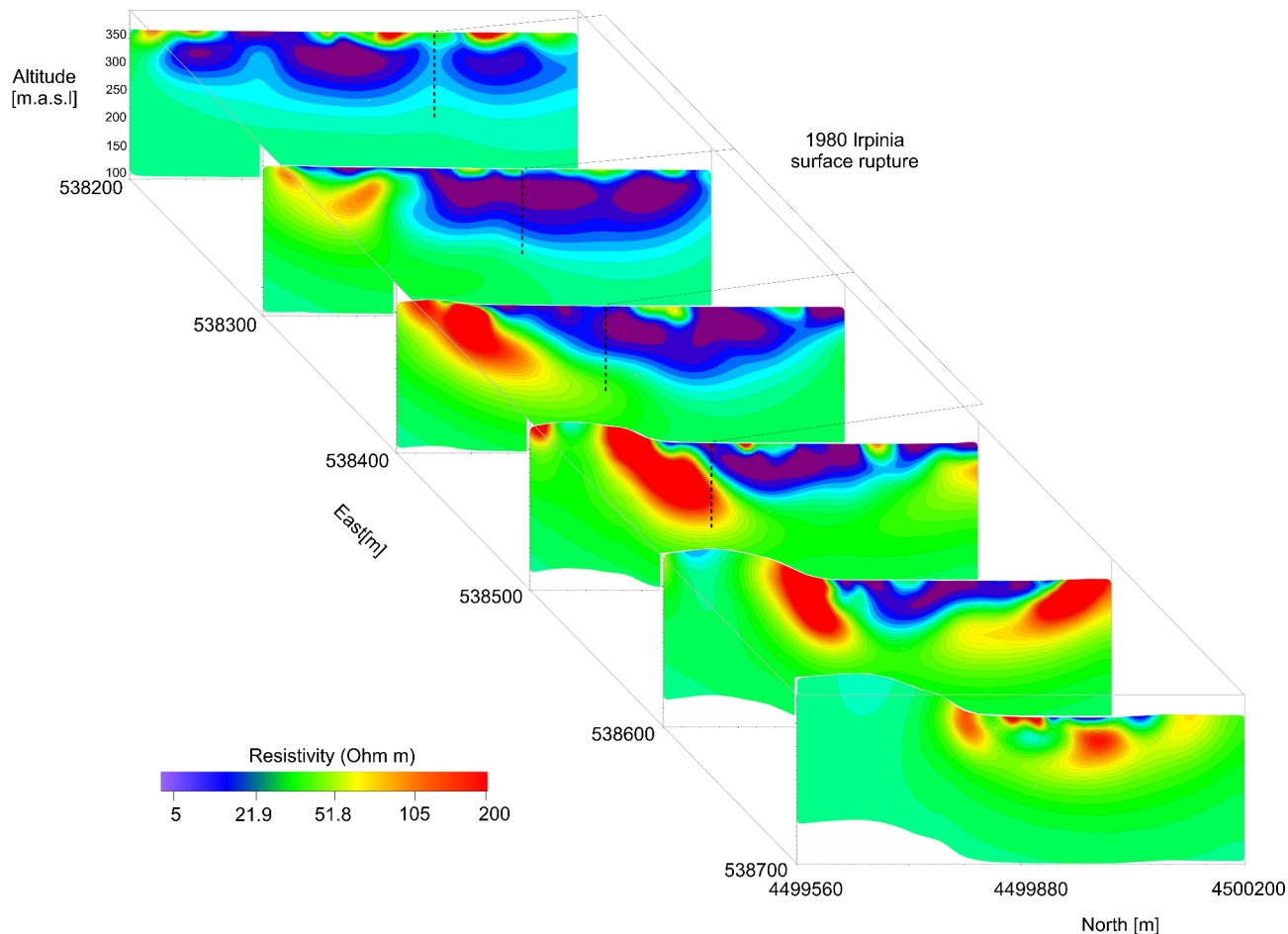
Fig. 10. YZ slices across the electric volume with the projection of the surface rupture that occurred during the 1980 Irpinia Earthquake in a dashed white line on the vertical sections. This figure was generated with ViewLab3D_64 (3.0, http://www.geostudiastier.it).

in southern Italy[70]. The terrain effect was estimated up to a 167 km distance using the Oasis Montaj software and two high-resolution DTMs: the local effect was computed using the TINITALY dataset[71] with a 10 m spatial resolution, while at greater distances we used the SRTM30 data[72] with an 80 m spatial resolution. The final map is shown in Fig. 11, where we can observe a clear agreement between the gravity anomalies and the main structural trends of the basin.

UAV magnetic surveys

A drone-borne magnetic survey was performed to check if magnetic data could be useful to define the basement geometry or even the fault trace across the Pantano basin. In this study, the potential utility of a magnetic survey may be supported by the presence of dispersed volcanic materials and volcanic tephra interspersed within the basin filling sediments, at various stratigraphic levels. As aforementioned, Munno and Petrosino[23] recognized the presence of 21 tephra layers in a 60 m borehole (which did not reach the bedrock) drilled in the depocentral area of Pantano Basin, relative to Phlegrean area eruptions (e.g., the Neapolitan Yellow Tuff and the Greenish Pumice eruptions). The tephra horizons, which appear regularly distributed throughout the core body, have a thickness ranging from 5 to 80 cm with a predominant sand-sized fraction[23]. Thanks to the measurements by Totaro et al[73]. and Crocitti et al[74]. magnetic susceptibility values ranging between 10 and 500×10^{-5} SI can be hypothesized for the tephra layers in the S. Gregorio Magno. In this geological context, we anticipate a magnetization contrast between the non-magnetic carbonate basement and the basin fill, which is enriched with volcanic materials. This contrast may also occur where faults displace magnetized filling layers. However, the survey area includes several anthropogenic structures, such as houses, a solar panel array, water drainage channels, and farming activity, which could generate intense artificial magnetic fields.

The magnetometer used in the drone-borne magnetic survey was the Geometrics Micro-Fabricated Atomic Magnetometer (MFAM) in the "Development kit" version. This magnetometer's high sampling rate of 1000 Hz allows for unaliased measurements of 50 Hz power line fields and accurate identification of high-frequency magnetic noise caused by the drone. The custom bird designed to house the MFAM consists of a polystyrene cover with a thin, rigid base made of a Nomex honeycomb sandwich panel (see Supplementary Fig. 9a). The total payload weight is ~2.0 kg. The drone used for the survey was an electric-powered DJI Matrice 600 pro
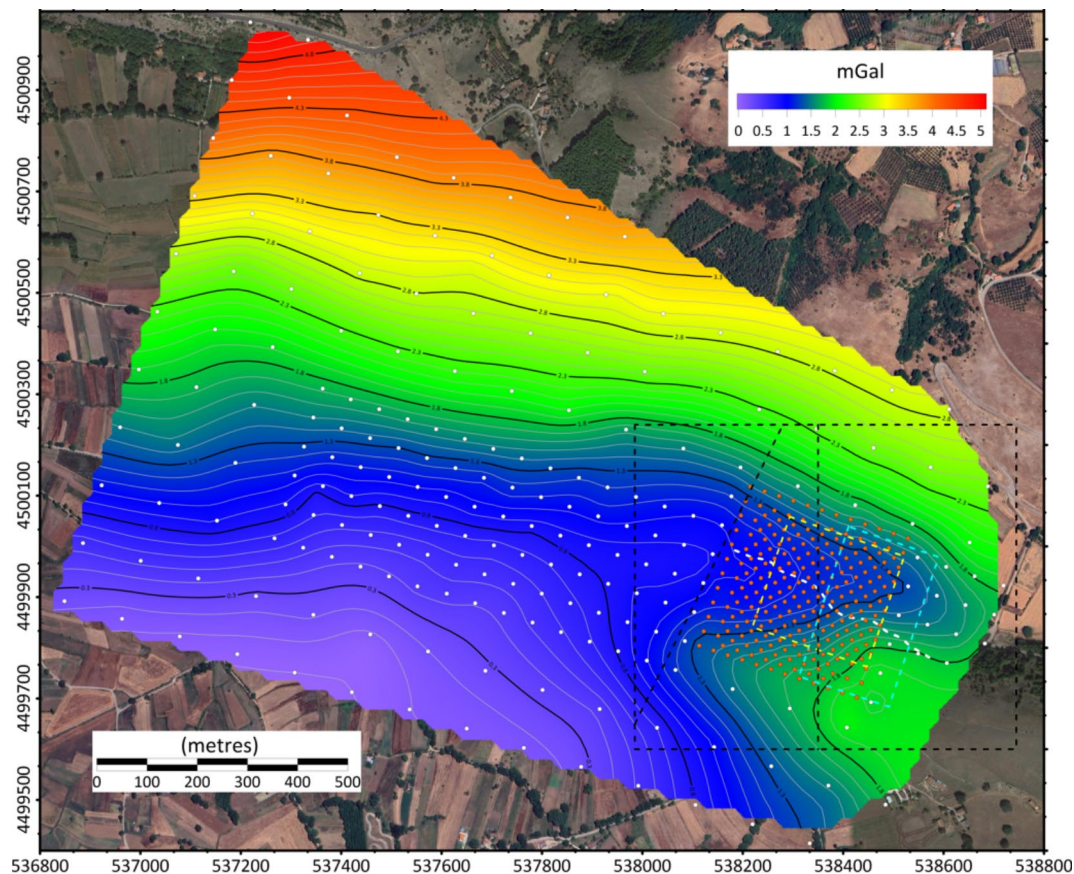
Fig. 11. Bouguer anomaly map of the area superimposed on satellite image from Google Earth Pro, v. 7.3.3 (https://www.google.com/earth/). Orange and white dots are the measurement performed in 2021 and 2023 respectively, the dashed white line is the surface rupture occurred during the 1980 Irpinia Earthquake. The black dashed rectangle is the region covered by the FullWaver measurements (depth slices shown in Figs. 8 and 9), with the two black dashed lines corresponding to the two vertical slices shown in Fig. 8. The yellow and cyan dashed boxes mark the areas covered by 3D seismic and resistivity measurements, respectively.

hexacopter. We minimized drone-induced magnetic interference by suspending the magnetic sensors 3 m below the UAV[75](see Supplementary Fig. 9b). The survey covered an area of approximately 1.5 km². Seventeen individual flights were conducted to cover the entire study area at an elevation of 40 m above ground level, with 38 parallel survey lines spaced 60 m apart and flown at a speed of 2 m/s. We used a digital elevation model (DEM) to plan the flight paths. The DEM was generated from photogrammetric data surveyed just before the magnetic acquisitions to ensure a constant altitude above the terrain. The acquired magnetic data were georeferenced using the UAV's GPS receiver (Fig. 12).

Ground Penetrating Radar UAV surveys

Ground Penetrating Radar (GPR) provides continuous high-resolution profiling of subsurface features, capable of locating objects and horizons at various scales. The GPR technique is increasingly applied in diverse fields such as architecture, engineering, environmental management, and mineral prospecting[76–79]. The electromagnetic pulse reflection used in GPR is based on the same physical principles as seismic reflection[80].

The Pantano basin is not an ideal place for GPR measurements, due to the nature of the sediments filling the basin and to a very shallow water table, even during summer. Therefore, the GPR survey was planned with the goal of imaging only the very near-surface structure (first 5–7 m) across the 1980 rupture and to verify the presence in the area of other splays of the IF with centimetric vertical offsets, which are beyond the resolution limit of the seismic survey. Consequently, many profiles (Fig. 13a) were acquired around the two trenches excavated by D'Addezio et al[36]., and the majority of the planned GPR acquisitions crossed the 1980 surface rupture.

The GPR instrument used was the COBRA Plug-in SE SE-70 monostatic antenna mounted on the DJI Matrice 600 Pro platform, as shown in Supplementary Fig. 10. To manage and control the UAV flight path, an IMU (Inertial Measurement Unit) and a GNSS (Global Navigation Satellite System) receiver were installed on board the drone, as well as a system that uses a data logger to record GPR data and control instruments from the ground station. In addition, the drone is equipped with a terrain-following radar altimeter that can accurately estimate the distance from the sensor's ground. The mission was planned using two complementary
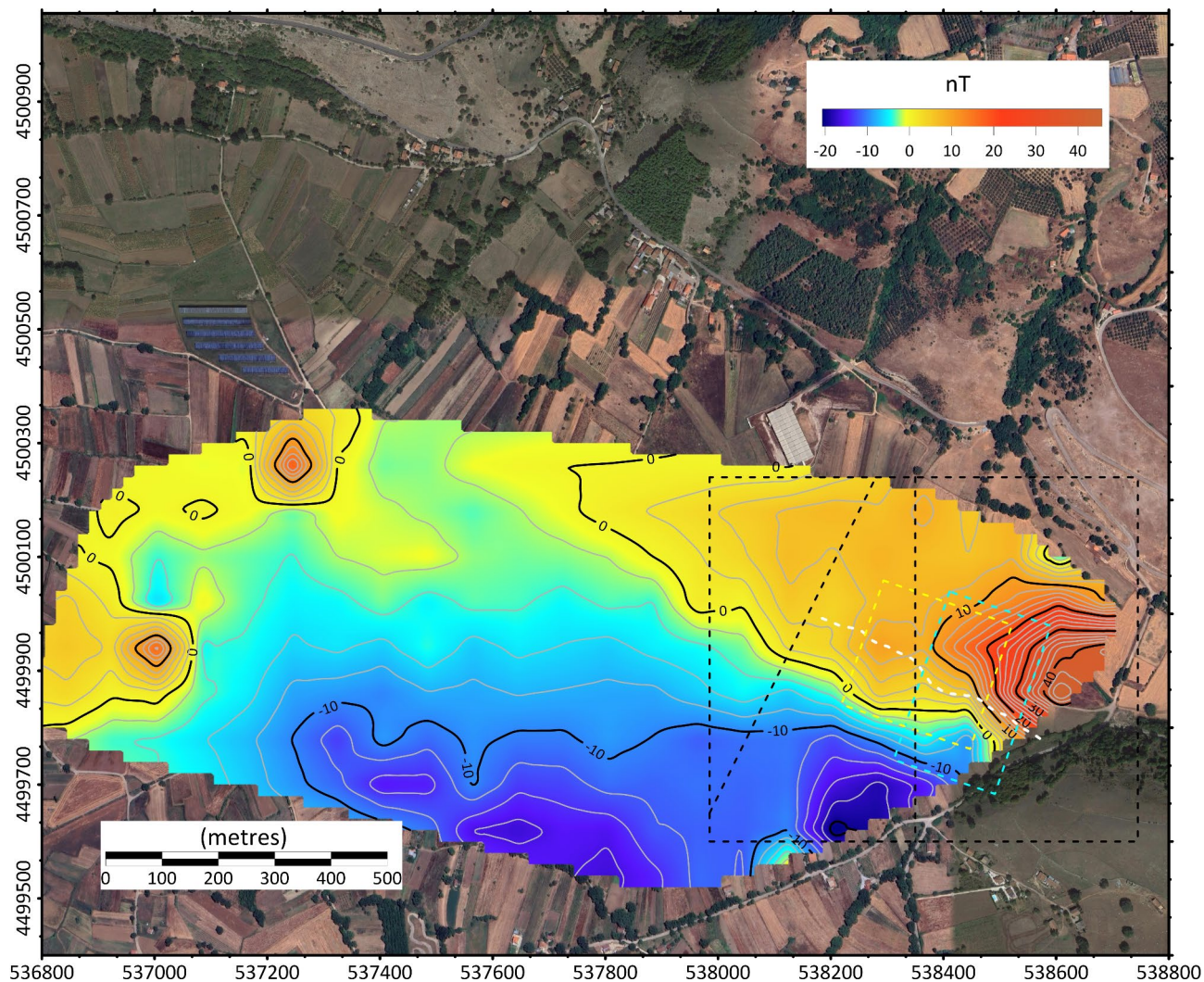
Fig. 12. Map of reduced to the pole of total field magnetic anomalies superimposed on satellite image from Google Earth Pro, v. 7.3.3 (https://www.google.com/earth/). The black rectangle is the region covered by the Fullwaver measurements, with the two black lines corresponding to the two profiles shown in Figure 8. The yellow and cyan boxes mark the areas covered by 3D seismic and resistivity measurements, respectively. The white dashed lines correspond to Irpinia Earthquake surface rupture.

software tools (Supplementary Fig. 10a-b): 1) Ugcs (Universal Ground Control Software) enterprise v.4.17 to plan the mission at a flight speed of 2 m/s[80]; 2) Ugcs-CPM (Custom Payload Monitor) v 3.4.1 to manage the radar altimeter in 'terrain following' mode, maintaining the antenna at 0.5 m above ground level, and to set the GPR parameters[82,83].

The GPR antenna has a center frequency of 80 MHz and a bandwidth of 120 MHz (2-140 MHz). In monostatic configuration, it achieves a nominal vertical resolution of 31 cm and a horizontal resolution of 88 cm. It can investigate subsurface structures down to a nominal depth of 50 m in ideal conditions (substrate with a relative dielectric constant of 5). The system collects 32,000 samples per second, boosting the signal-to-noise ratio to 45 dB, surpassing traditional GPR systems in penetration capacity. This eliminates the 'ringing' effect, and the low-voltage transmitter reduces power consumption. The low-frequency antennas enable their use in ground/air coupling operations on any terrain.

We have taken several critical steps in processing GPR data, to ensure accurate subsurface imaging and interpretation. Initially, we applied a "dewow" filtering to remove low-frequency noise and background removal to enhance signal clarity[84]. Following this, we applied a time-zero correction to consistently align the start of the radar signal[85]. This correction ensures that the depth calculations are accurate across the entire dataset. Furthermore, we applied amplitude correction and signal gain adjustments to compensate for the natural attenuation of the radar signal with depth[86]. Finally, GPR data have been depth converted using a constant velocity of 12.5 m/ns.

Figure 13 shows two acquired GPR profiles, the one in Fig. 13b has been acquired in a standard procedure, i.e., moving the 80 MHz antenna on the ground, while the other in Fig. 13c was acquired using the same antenna mounted on the DJI Matrice 600 Pro. Both profiles cross the Irpinia Earthquake surface rupture (red
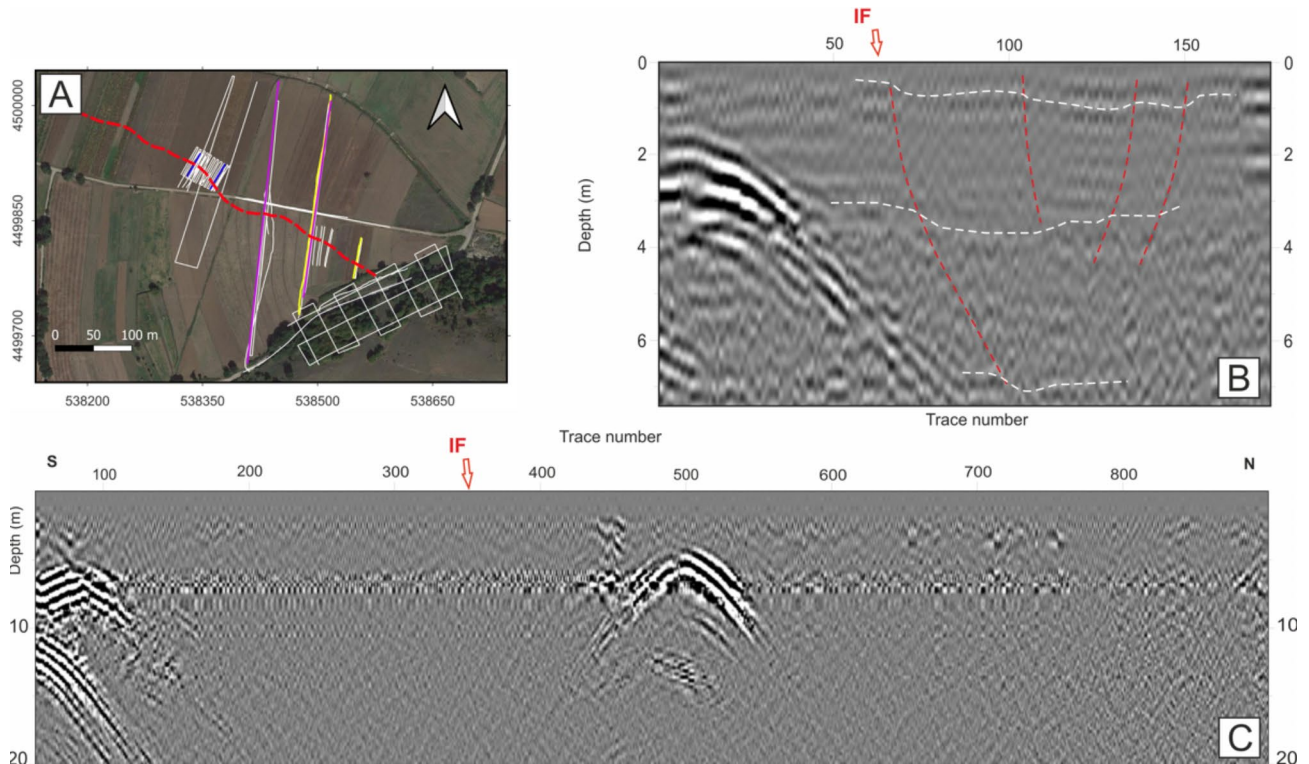
Fig. 13. The white segments in the map (A) show the traces of the acquired GPR profiles, some overlapping with seismic profiles Pantano_3 and Pantano_4 (purple lines) and others located around the two trenches of D'Addezio et al[36]. (blue lines); most of them cross the Irpinia Earthquake surface rupture (red dashed line). The profiles colored in yellow are the radargrams shown in (B) and (C).

dashed line in Fig. 13a); additionally, the longer profile also crosses a paved road with some underground pipes (corresponding to the diffraction in the middle of the radargram) the profile in Fig. 13b shows overall a better signal-to-noise ratio, allowing us to see some rupture-related features we will discuss in the next paragraph.

CO2 flux survey

The CO_2 fluxes from the ground to the atmosphere were determined at 81 measurement stations along the 1980 fault scarp and its surroundings. All measurements were completed over three days in July 2023 under dry weather conditions to minimize any interference from soil moisture variations[87]. The measurement stations were distributed across the target area with a regular spacing of 30 m, which was deemed sufficient to detect flux spatial variations due to the presence of the fault (Fig. 14). The flux was determined using a time-integrated 6-channel selective infrared gas analyzer (ECOPROBE 5, RS DYNAMICS) coupled to a static accumulation chamber, a bell-shaped hollow container made of steel with an internal volume of 4920 cm³ and a circular opening with a diameter of approximately 28 cm. Basically, the ECOPROBE 5 is connected to the accumulation chamber through a closed circuit using two tubes: one drives the gas from the chamber toward the analyzer, and the other returns the gas to it after it has been analyzed. The chamber is internally equipped with a fan (power supplied by a 6-volt battery sitting on the top of the device) added to the system to favor a homogeneous gas distribution inside its volume. Before starting operations, the vegetation cover was removed at each measuring station, and the topsoil was gently leveled. The chamber was positioned with the opening facing the ground and sealed by pressing its edge against the soil.

An automatic recalibration was conducted before starting measurements at each station, using atmospheric CO_2 levels as a reference to guarantee the reliability of the results. The CO_2 concentrations were measured ten consecutive times at regular intervals of one minute. During individual measurements, gas was extracted from the chamber at a rate of 1.25 L per minute for 20 s, and the ECOPROBE 5 provided an average value derived from 40 consecutive readings. Following the completion of ten successive measurements at each monitoring station, the relative soil flux was computed by assessing changes in CO_2 concentration over the whole 10-minute measuring period, applying the following equation (Eq. 2):

$$f CO_2 = (\Delta CO_2)/\Delta_t \cdot V/A \qquad (2)$$

Where:

- $f CO_2$ is CO_2 flux emitted from the ground (in mg·m^{-2}h^{-1});
- ΔCO_2 is the difference in CO_2 concentrations between two consecutive measures (in mg·m^{-3}),
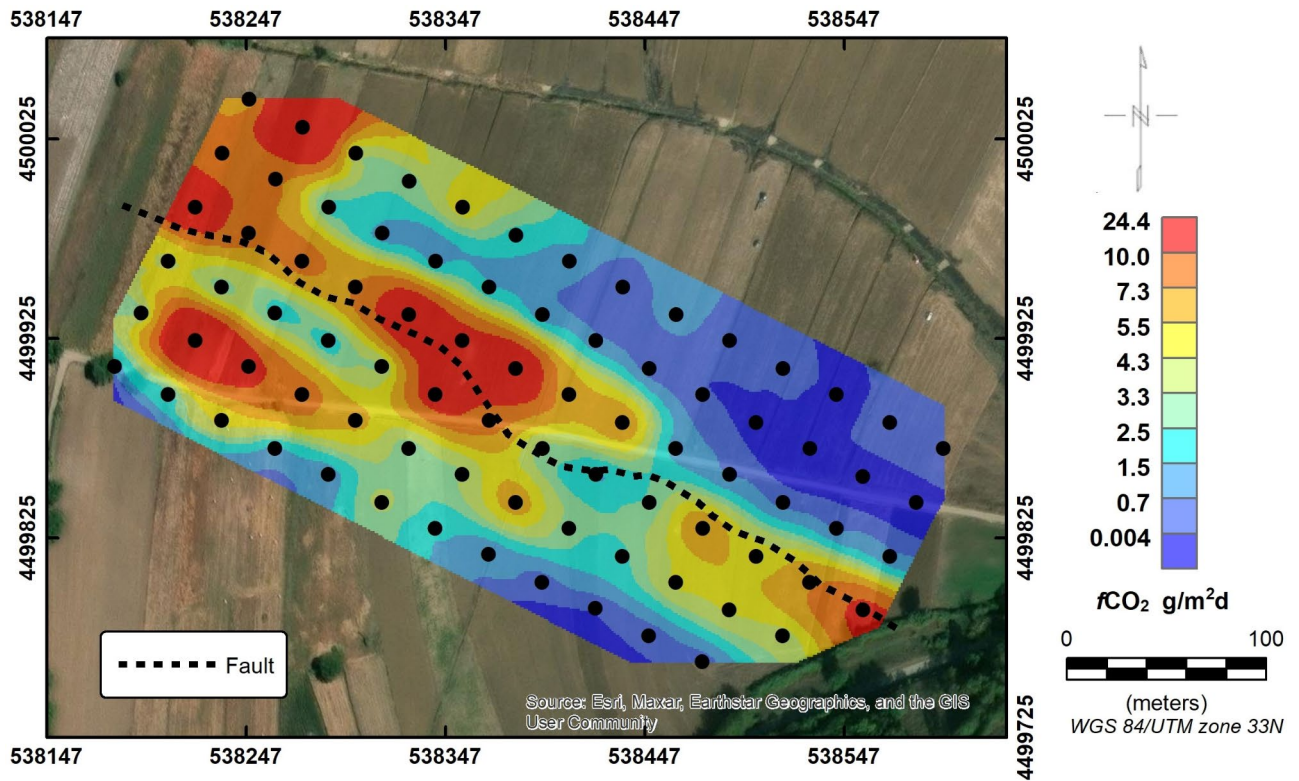
Fig. 14. Tthe CO_2 fluxes from the ground to the atmosphere along the 1980 Irpinia Earthquake scarp and its surroundings displayed on satellite image from Google Earth Pro, v. 7.3.3 (https://www.google.com/earth/). The 81 measurement stations (black dots) were distributed across the surface rupture occurred during the 1980 Irpinia earthquake with a regular spacing of 30 m.

- Δ_t is the time interval elapsed between two measures (expressed in hours, h),
- V is the volume of the chamber (in m³).
- A is the surface covered by the chamber opening (expressed in m²).
- The estimated hourly flux data, converted into their corresponding daily rate to facilitate comparison with the literature, were georeferenced and mapped in ArcMap (Fig. 14).

Results & discussion

We begin this section by presenting the results from the seismic experiment. Slices from the 3D seismic cube (Fig. 4) demonstrate a high-quality imaging of the near-surface of the Pantano basin. A highly reflective package is clearly visible in the hanging-wall of the 1980 fault scarp, while a much less reflective package appears in the footwall due to a shallower carbonate basement. In Fig. 5B, we present a detailed interpretation of the oblique random line of Fig. 4, and we compare it with the 2D profile Pantano_3 presented by Bruno et al[19]. Uninterpreted data can be seen in Supplementary Fig. 3. Based on the outcomes of the 3D survey, we provide an updated interpretation of profile Pantano_3 of Bruno et al[19]. For the seismic stratigraphic interpretation, we followed Bruno et al[19]., who defined four seismic units based on distinct seismic velocities, patterns, and reflective configurations. However, our interpretation was further refined using available borehole data from Aiello et al[21]. paleoseismological surveys[36], seismic tomography[19], and electrical resistivity data[88].

At the bottom of the seismic volume, we identify the top of the carbonate substratum as a high-amplitude, low-frequency reflector. This reflector marks a high P-wave velocity (Vp 3000–4500 m/s) and a reflection-free volume below (i.e., Unit 1), characteristic of massive carbonate units and distinct from the unconformable, highly reflective sedimentary package above (Units 2–4). The carbonate substratum lies approximately 60 m deep in the footwall and has a concave shape in the hanging wall, reaching a maximum depth of ~ 120 m.

Unit 2, characterized by a transparent to poor reflective character; chaotic patterns and by high P-wave velocity (2000–3000 m/s), is interpreted as Middle to Upper Pleistocene cemented carbonate slope deposits, particularly in the fault footwall, where it exhibits a thickness of nearly 25 m. In the hanging wall, this unit thickens to up to 70–80 m and shows more organized, dipping reflections with a divergent pattern and lower P-wave velocity, likely indicating an alternation of coarse and fine-grained deposits.

Unit 3, with P-wave velocities between 1600 and 2000 m/s, appears as a highly reflective and continuous package in the fault's hanging wall, consistent with lacustrine deposits as indicated by the well stratigraphy of Aiello et al[21]. In contrast, Unit 3 in the fault's footwall, similar to Unit 2, exhibits low reflectivity, especially along the oblique line, and displays hummocky clinoform configurations on the more detailed Pantano_3 profile, suggesting deposition in a higher-energy environment, likely continental slope deposits. Finally, Unit 4 located

at the upper boundary of the seismic cube, is characterized by low P-wave seismic velocities (Vp < 1500 m/s) and low resistivity (< 30 Ohm m, according to Troiano et al[88].). Compared to the 2D seismic profile by Bruno et al[19]., which offers better resolution near the surface (< 25 m depth, Fig. 5a), Unit 4 is less clearly defined in the seismic volume (Fig. 5b). Based on trench[3,36] and well stratigraphy data[21], we associate Unit 4 to a package of fine sediments, including lacustrine deposits and colluvium rich in volcanic materials, transitioning laterally into coarser slope deposits at the southern edge of the basin on the upthrown side of the Pantano-Ripa-Rossa Fault.

Based on chronostratigraphic analysis performed on well data by Aiello et al[21]., we can infer the ages of our Quaternary seismic units. Unit 2 dates to the Middle Pleistocene, Unit 3 to the Late Pleistocene, and Unit 4 spans from the upper Late Pleistocene to the Holocene. The tilting and lateral growth of Units 2 and 3 towards the fault, clearly visible on the oblique random line in Fig. 5b, indicate syn-sedimentary activity. The thickening and wedging of Unit 2, and to a lesser extent Unit 3, on the downthrown side of the fault (Fig. 5b) suggest that fault activity influenced the deposition of these units.

The Pantano-Ripa-Rossa Fault is identified through (see also Bruno et al[19].): (1) a sudden change in the reflection patterns within the fault zone; (2) distinct truncations in reflections within the depth range of 30–125 m; (3) growth strata in the fault hanging wall, dipping towards the fault surface. The fault zone surface projection matches the 1980 co-seismic scarp and faulted deposits exposed in the trenches of D'Addezio et al[36]. The fault apparent dip is between 58° and 68°, in good agreement with a 70°-dipping fault plane exposed in the trenches[36]. The top basement offset, measured across the fault zone, yields a cumulative throw of ~ 60–72 m, more than the 29–38 m estimated by Bruno et al[19]. on profile Pantano_3 (yellow dashed line in Fig. 5a). In our new re-interpretation of Pantano_3, based on the comparison with 3D data, we moved the top of the carbonates in the fault hanging wall 25 m deeper. We recall that profile Pantano_3 was acquired using buffalo-gun shots. The comparison with the new vibratory 3D data suggests that the misinterpretation of the carbonate substratum in the fault hanging wall was due to the use of a weaker source with a lower penetration capacity.

Assuming a 0.3 mm/yr vertical slip rate reported by D'Addezio et al[36]. and using the total vertical slip estimated at the top of carbonates, we speculatively estimate the inception age of Pantano-Ripa-Rossa Fault to be around 200–240 ka (Middle Pleistocene), ~ 100 ka older than the age previously assessed by Bruno et al[19]. However, a reliable throw measurement is complicated by the fact that the Pantano-Ripa-Rossa Fault displaces a marine carbonatic substratum with an articulated morphology (i.e., paleovalley), likely pre-dating the fault inception. As a result, the measured top of the carbonates in the hanging wall may not correspond to equivalent levels in the footwall, potentially leading to a misestimation of the fault throw.

Given the challenges in accurately measuring fault throw, an alternative estimation for the age of the Pantano-Ripa-Rossa Fault's inception can be made using a sedimentation rate of 0.56 mm/yr for the Pantano Basin, derived from well chronostratigraphic data by Aiello et al[21]. In the fault's hanging wall, ~ 70 m of Late Pleistocene deposits (Units 3–4), if accumulated at a constant rate of 0.56 mm/yr, suggest that their base dates back to ~ 250 ka, potentially marking the inception of fault activity. Additionally, if the base of Unit 3 corresponds to the Tyrrhenian stage (~ 128 ka), the observed maximum offset of ~ 35 m between Units 2 and 3 could suggest an average slip rate of ~ 0.27 mm/yr, consistent with D'Addezio et al[36].

Figure 6 shows a few depth slices of the electric cube, revealing low resistivity in the basin infill, ranging from 4 to 20 Ohm m, values being typical of saturated or partly saturated loose sediments. The resistivity distribution is influenced by the Pantano-Ripa-Rossa Fault, with the fault's footwall (to the south) showing slightly higher resistivity than the hanging wall. This difference is most evident in horizontal sections at depths of 45 and 52 m, though resolution decreases with depth due to filtering of apparent resistivity data to remove the effects of underground electrical cables. At shallower depths, the resistivity distribution is more complex, likely reflecting variations in porosity and the impact of the fault on subsurface water drainage and sediment permeability.

The higher-resolution 3D electrical survey conducted in the middle of the basin (Fig. 2) does not reach the carbonate basement, and this contributes to the limited and relatively low resistivity range observed. In contrast, the lower-resolution 3D FullWaver survey (Figs. 8, 9 and 10) penetrates to about 150 m, reaching the fractured carbonate basement, characterized by resistivity values exceeding 200 Ohm m. To better highlight the variability within the basin infill, the resistivity range in the figures is clipped at 200 Ohm m. Part of the survey (Fig. 7) was conducted over carbonate outcrops, enabling calibration of the electrical data against the basement's resistivity.

The horizontal and vertical slices of the 3D FullWaver model (Figs. 8, 9 and 10) clearly delineate the basin infill as a low-resistivity volume and distinctly show the contact between the basin infill and the carbonate basement to the north and south. The basin-fill loose sediments exhibit resistivity values ranging from 5 to 30 Ohm m, consistent with the 3D high-resolution electrical survey (4 to 20 Ohm m). The differences are likely due to the varying resolutions of the surveys and the different acquisition times (July 2021 for the 3D survey and September 2023 for the FullWaver survey), which may have affected surface sediment saturation levels. Resistivity values above 200 Ohm m are characteristic of fractured, water-saturated carbonates.

The constant-depth electrical slices in Fig. 9 suggest that the basin edge follows structural trends in the NW-SE and NE-SW directions, aligned with the carbonate outcrops to the north and south of the study area. The studied basin volume has a triangular shape with straight edges, narrowing towards the east, as further discussed in the gravity data analysis below. Within the basin, the FullWaver survey reveals significant heterogeneity in electrical properties, though the FullWaver model has lower resolution than the previous 3D electrical model. At depths of -60 m and especially −80 m, the basin appears to split into two depocenters These depocenters are clearly affected by the surface rupture associated with the 1980 earthquake, marked by a dashed white line in the images.

The N-S oriented vertical slice represented in Fig. 8 reveals that approximately 30 m south of the surface rupture (marked by the dashed white line), the carbonate basement experiences a 50–60 m vertical offset, likely caused by the Pantano-Ripa-Rossa Fault. This supports the findings of the 3D seismic reflection survey discussed earlier. Another sudden 20-m uplift of the carbonates is observed 50 m south of the first splay, leading to the

basement outcropping further south. This abrupt elevation is likely due to the southern splay of the PSGM fault system, which bounds the Pantano Basin (Fig. 1B). These splays concur to submerge the carbonate basement by ~ 120 m toward the basin's center, a value consistent with seismic data. The resistivity then rises abruptly to the north at metric 540, possibly outlining a northern conjugate splay of the PSGM fault system or more cemented slope deposits. The model outlines a bowl-shaped basin, approximately 350 m wide and up to 120 m deep in the investigated profile, encompassing the entire lateral extent of the 1980 surface rupture. The vertical N-S electric slices in Fig. 10 confirm the significant lateral heterogeneity in electrical properties within the basin, reflecting the complexity of the infill (i.e. alternating lacustrine deposits, alluvial fans, and dense to cemented slope debris from Units 2, 3, and 4). This heterogeneity may contribute to lateral variations in wavelet polarity across the seismic boundaries of Units 2, 3, and 4, making reflector picking in the 3D seismic volume more challenging.

The electric slice at X coordinate 538,500 of Fig. 10 roughly aligns with profile Pantano_3 in Fig. 5a, with a minor difference in strike of ~ 8° (see also Fig. 3). Meanwhile, the oblique line in Fig. 5b falls between electric slices at X coordinates 538,300 and 538,600, intersecting the IF surface rupture at 538,450. Notably, the seismic and electric images exhibit very similar geometries of the basin and the fault zone. Additionally, the electric slices in Fig. 10 highlight significant geometrical changes affecting both the Pantano-Ripa-Rossa and the southern splay of the PSGM Fault System along the E-W direction, a feature also observed, on a smaller scale, within the 3D seismic cube.

The map depicted in Fig. 11 shows the Bouguer anomaly of the investigated area, with measurement stations marked by dots. Gravity data were collected more densely along the 2D seismic profiles and within the 3D electric and seismic volumes to allow, in a future step of data analysis, to use them as a constraint for gravimetric basement modeling[89]. The Bouguer anomaly map displays a northward increase, which can be roughly associated with the depth of the carbonate basement, showing low gravity values toward the basin center (south) and higher values in the north, where the basement outcrops. This suggests that the Bouguer anomaly is primarily influenced by the thickness of the basin fill sediments, which have a lower density than the carbonate rock. Consequently, the anomaly amplitude can provide a rough estimate of the basin's depth and the underlying carbonate basement's morphology.

However, a closer comparison of the topographic and geological maps with the Bouguer anomalies reveals that the gravity trend does not perfectly align with the carbonate outcrops or the dense carbonate debris outcrops. Additionally, the gravity low appears to shift southward relative to the geometric center of the basin. This suggests the presence of a regional gravity component superimposed on the main density contrast between the basement and the basin fill. Removing this regional component is complex and lacks a standard method, requiring geological and structural knowledge of the area[90]. Another possibility is that the basin has an asymmetric shape at depth, being deeper southward.

The Bouguer anomaly trend is regular north of the 1.8 mGal contour line, progressively increasing as it moves northward. However, south of the 1.8 mGal contour line, the trend becomes more complex, showing a minimum that wedges eastward near the 1980 surface rupture. This pattern is consistent in shape with the results of the FullWaver electric survey (Fig. 9). South of the 1980 rupture, the Bouguer anomaly peaks at the carbonate outcrop of Mt. Ripa Rossa (Fig. 1B), before decreasing westward and southward. This suggests that the carbonate wedge forming Mt. Ripa Rossa extends westwards beneath the basin. It is worth noting that the Pantano-Ripa Rossa Fault and the southern splay of the PSGM fault system intersect at Mt. Ripa Rossa ridge (Fig. 1B). Therefore, short-wavelength features of the Bouguer anomaly trend, visible in this more densely sampled part of the map, are likely low-magnitude gravity perturbations caused by the Pantano-Ripa Rossa Fault and the southern splay of the PSGM fault system.

Overall, the qualitative interpretation of the basin extent, based on the Bouguer anomaly, is consistent with the findings from the seismic and FullWaver surveys. The shape of the anomaly aligns well with the morphology of the submerged carbonate basement, as revealed by seismic and electric data. It suggests that the basin floor in the area of the surface rupture may have a morphology interpretable as a paleo-valley, which appears to narrow eastward just north of the rupture.

The magnetic survey covered a smaller portion of the basin compared to the gravimetric survey, due to logistical challenges that prevented the collection of additional data above the carbonate outcrops in the surveyed area, both to the south and north of the basin, which would have been valuable for better assessing the spatial variation of tephra thicknesses from the outcrops towards the basin's center. Figure 12 shows the reduced to the pole Total Field Anomaly (TFA) map. The map presents a maximum amplitude variation of ~ 60 nT, ranging from ~ − 20 to 40 nT. As the magnetic map is reduced to the pole, the magnetic highs and lows are approximately positioned above their sources. This will happen if the source magnetization direction is correctly selected when performing the reduction to the pole. In our case, we assumed that there is no remnant magnetization, so that the magnetization is purely induced, having a direction parallel to that of the International Geomagnetic Reference Field in this area (Declination: 3°; Inclination: 57°).

A WNW-trending magnetic high is present in the north-eastern part of the area, and a similar trending magnetic low is present south of the magnetic high. These trends align with the strike of the surface rupture. Both anomalies have their highest intensity just at the edge of the surveyed area so that, unfortunately, these anomalies are not seen in their entirety in the map of Fig. 12 . Other localized anomalies are present in the western part of the area and can be related to anthropic disturbances generated by homes, cars or tractors, metallic bridges, etc.

The magnetic anomaly pattern seems to be roughly related to the thickness of the sediment filling the plain, with higher values where the thickness decreases. In fact, a decrease in the depth of the carbonate basement toward the north is suggested by gravity data and is seen in seismic and electric surveys. As the carbonates should be practically non-magnetic, this observation may imply the presence of a significantly magnetized layer of volcano-clastic sediments near the bottom of the basin. In fact, as we mentioned before, the basin fill contains

an intermittent input of volcanic components, generating individual layers of magnetized sediments. Presently, this hypothesis seems to be the most probable, although an extension of the magnetic survey to the east and to the south might be necessary to verify its correctness.

Following the gravity survey, Ground Penetrating Radar (GPR) data were collected to provide detailed subsurface insights above the surface rupture (Fig. 13). To evaluate the drone-mounted GPR system, control radargrams were acquired using a standard ground-based setup, which provided a clearer signal-to-noise ratio, as shown in the example radargrams in Fig. 13b-c. The profile in Fig. 13b indeed achieved a penetration depth of ~ 7 m and shows, on its left side, a reflector dipping toward the center of the profile, which can be tentatively correlated to the dipping carbonate bedrock that outcrops a few meters to the left end of the radargram.

Sub-horizontal reflectors onlapping above it show at least four consistent and realistic inflections ranging from 50 to 110 cm, one just below the 1980 surface rupture (at 60 m), another found at 105 m and other two across possible conjugate fault splays at 130 and 150 m; Such vertical offsets, consistent across all the sub-horizontal reflective package define four probable steep fault segments dipping to the north and to the south. Importantly, the magnitude of displacement aligns with the vertical offset observed at the surface during the 1980 (50 cm) and with offsets of up to 2 m found by D'Addezio et al[36]. in trenches 3–4.

Despite promising results from ground-based radargrams, most of the drone-mounted GPR data exhibited poor signal-to-noise ratios, with diffractions from man-made objects being the most prominent features (e.g., Fig. 13c). Unlike successful GPR surveys in the nearby Piano di Pecore basin under similar geological and soil conditions[91], the poor performance at Pantano is attributed to a shallower water table and inconsistent antenna height and azimuth due to bearing and altitude errors from the drone.

Finally, we conclude our discussion on the results of this multidisciplinary campaign by presenting the results of sampling the CO_2 fluxes from the ground to the atmosphere along the 1980 Irpinia Earthquake surface scarp and its surroundings. The daily CO_2 flux data in Fig. 14 ranges from a minimum value of 0.01 g/m²d to a maximum of 32.88 g/m²d with an average value of 3.97 g/m²d and a median of 0.32 g/m²d, showing an asymmetrical markedly right-skewed distribution (see Supplementary Fig. 11). The cumulative frequency curve (see Supplementary Fig. 12) shows the existence of three populations in the dataset: one featuring a very low slope in the range between 0.01 and 1.5 g/m²d, one including value up to 8.8 g/m²d and the latter characterized by values up to the maximum (32.88 g/m²d).

In line with the values of the statistical location indices reported above and the distribution plots, the interpolated map of CO_2 fluxes (Fig. 14) shows a complex spatial pattern with (a) values below 1.5 g/m²d mostly concentrated in the eastern sector of the map far away from the reported 1980 Irpinia Earthquake scarp trace and along the southern edge of the investigated area, (b) very high values (from 7.3 g/m²d up to 24.4 g/m²d) mostly located in correspondence of the fault trace and two small areas of limited extension on the north-western and south-western sectors of the investigated area, (c) intermediate values (between 1.5 to ~ 7.3 g/m²d) characterizing the transition zone between lower and higher fluxes.

The lower data interval can be considered as a reference for the local baseline of the CO_2 flux predominantly associated with the biological activity of the pedological cover[92], as also reported for other non-volcanic areas of the Campania region[93]. On the other hand, values belonging to the highest CO_2 concentration range can be seen as an anomalous statistical population indicative of the presence of the deeper seismogenic structure connected to the surface rupture of the 1980 Irpinia Earthquake; in this regard, the fluxes falling in the intermediate range of values are probably representative of a stress zone crossed by secondary lineaments connected with the main fault acting as the primary gas source[94].

Notably, soil gas measurements of different gas species, including CO_2, performed by Ciotoli et al[95]. across another segment of the of the MMFS in the area of Piano di Pecore, in the northern Mount Marzano massif, also found anomalies that are aligned with the NW-SE trending coseismic rupture of the 1980 earthquake, as well as along the southern border of the plain where a hidden, E-W striking fault is inferred[95].

Conclusions

The multidisciplinary investigation conducted over the past three years at the Pantano di San Gregorio Magno basin as part of the TESIRA project has provided significant insights into its geophysical characteristics. Through a multi-scale and multi-resolution strategy that integrates geophysical and geochemical surveys across the full extent of the 1980 Earthquake surface rupture in the Pantano Basin and surrounding areas, we have gained a clearer understanding of the near-surface geometry, stratigraphy, and active fault strands responsible for the basin's development.

The seismic, gravity, and electrical data converge in revealing a consistent picture of the basin and fault zone, highlighting the three-dimensional characteristics of the investigated fault strands. Additionally, the geometrical complexity of the basin revealed by our surveys, highlights the limitations of relying solely on 2D profiling or a single methodology for exploration in such environments. Even with careful planning, an approach centered on multiple 2D profiles may fail to fully capture the subsurface fault geometry, potentially leading to an incomplete or overly reductive depiction of the subsurface settings.

An illustrative example is the 2D survey across the Pantano - Ripa Rossa Fault conducted by Bruno et al[19]. Although this survey was planned based on a thorough review of surface geological and morphological information, and aligned almost orthogonal to the 1980 surface rupture, a comparison with our 3D data reveals significant discrepancies. The in-depth geometry of Units 2 and 3, and the thickening, wedging and back-tilting of these units towards the fault, was only partially captured by Bruno et al[19]. The limitations of 2D migration in such a 3D setting arise from its inherent inability to resolve lateral variations that are not in the profile plane. These variations can only be accurately imaged through 3D migration. Moreover, our interpretation of the seismic data suggests that the cumulative deformation produced by the Pantano-Ripa Rossa Fault may be greater

than the previous estimation by Bruno et al[19]. and that the inception of this fault could be dated the Early-to-Middle Pleistocene (~ 200–250 ka).

At Pantano Basin, sedimentation rates balanced the subsidence caused by fault activity[21]. However, the Pantano-Ripa Rossa Fault, located centrally within the basin, contributed only a minor portion to the accommodation space generated by faulting, with the main contribution coming from the PSGM fault system, as indicated by FullWaver data. This data, consistent with seismic findings, also suggests that the Pantano-Ripa Rossa Fault and the nearby PSGM Faults bounding the basin to the north and south are geometrically connected.

While surface evidence along the MMFS suggests small cumulative fault throws, crustal-scale cross-sections and seismological data may indicate larger throws. According to Ascione et al[96]., this discrepancy is due to decoupling between deep and shallow fault zones within a tectonic mélange between the Lagonegro Basin units and the deeper Apulian Platform carbonates. However, the consistent CO_2 anomalies we found along the Pantano-Ripa Rossa Fault, along with those identified by Ciotoli et al[95]. across the Monte Marzano segment of the MMFS, suggest a direct connection between the shallow ruptures and the deep seismogenic structure. This hypothesis has been recently reinforced by Feriozzi et al[97] and Bello et al[15], based on the analysis of prevailing structural trends, interpretation of vintage seismic profiles, tomographic velocity models and recent background seismicity.

Overall, the integrated geophysical and geochemical data acquired under the TESIRA project provide a comprehensive understanding of Pantano basin's subsurface structure, from small to large scale, and its evolution driven by fault dynamics. However, not all acquired data yielded equally useful results. The decision to use drone-mounted equipment for the GPR survey proved to be suboptimal. This is evident when comparing the radargrams recorded by the drone to those from ground surveys. We have identified the probable causes of these shortcomings, such as the presence of a shallow water table, the need for a lower frequency setting of the antenna, and the potential benefit of flying at a lower altitude or eliminating the terrain-following mode in the flight planning. By sharing our experience, we aim to provide insights for future improvements. Despite these challenges, aerial surveys by drone still hold significant potential for conducting quick and cost-effective surveys of fault-bounded basin areas, especially where logistical and permitting issues may limit the feasibility of ground surveys.

Data availability

The datasets analyzed during the current study are available from the corresponding author on reasonable request.

References

1. Galli, P., and Peronace, E., (2014). New paleoseismic data from the Irpinia Fault. A different seismogenic perspective for southern Apennines (Italy). Earth-Sci. Rev. 2014, 136, 175–201.
2. Pantosti, D., and Valensise, G., (1990). Faulting mechanism and complexity of the November 23, 1980, Campania-Lucania earthquake, inferred from surface observations, J. Geophys. Res., 95(15), 319– 341, 1990.
3. Pantosti D., G. D'Addezio, and Cinti, F.R., (1993). Paleoseismological evidence of repeated large earthquakes along the 1980 Irpinia earthquake fault. Annals of Geophysics, 36/1, 321–330.
4. Bernard, P., and Zollo, A. (1989). The Irpinia (Italy) 1980 earthquake: detailed analysis of a complex normal faulting. J. Geophys. Res 94, 1631–1647. doi:https://doi.org/10.1029/jb094ib02p01631
5. Pingue, F., De Natale, G., and Briole, P. (1993). Modelling of the 1980 Irpinia earthquake source: constraints from geodetic data. Ann. Geofisc 36, 27–40. doi:https://doi.org/10.4401/ag-4296
6. Westaway, R., and Jackson, J. (1987). The earthquake of 1980 November 23 in campania-basilicata (southern Italy). Geophys. J. Roy. Astron. Soc 90, 375–443.
7. Amoruso, A., Crescentini, L., Di Lieto, B., Scarpa, R., (2011). Faulting mechanism of the Campania–Lucania 1980 earthquake, Italy, from high-resolution, 3D velocity structure, aftershock relocation, fault-plane solutions, and post-seismic deformation modelling, Annals of Geophysics, 54, 6, https://doi.org/10.4401/ag-4984.
8. Westaway, R. and Jackson, J., (1984). Surface faulting in the southern Italian Campania-Basilicata earthquake of 23 November 1980, Nature, 312, 436–438, https://doi.org/10.1038/312436a0.
9. Blumetti, A.M., Esposito, E., Ferreli, L., Michetti, A.M., Porfido, S., Serva, L., Vittori, E., (2002). New data and Reinterpretation on the November 23, 1980, M 6.9 Irpinia - Lucania Earthquake (Southern Apennines) Coseismic Surface Effects, STUDI GEOLOGICI CAMERTI. NUOVA SERIE
10. Ascione, A., Mazzoli, S., Petrosino, P., Valente, E., (2013). A decoupled kinematic model for active normal faults: insights from the 1980, MS = 6.9 Irpinia earthquake, southern Italy. GSA Bulletin, 125 (7–8), 1239–1259. https://doi.org/10.1130/B30814.1.
11. Galadini, F., Galli, P., (1999). The Holocene paleoearthquakes on the 1915 Avezzano earthquake faults (central Italy): implications for active tectonics in the central Apennines. Tectonophysics, 308, 1–2, 143–170, https://doi.org/10.1016/S0040-1951(99)00091-8.
12. Volatili, T., Agosta, F., Cardozo, N., Zambrano, M., Lecomte, I., & Tondi, E. (2022). Outcrop-scale fracture analysis and seismic modelling of a basin-bounding normal fault in platform carbonates, central Italy. Journal of Structural Geology, 155, 104515.
13. Patruno, S., and Scisciani, V., (2021). Testing normal fault growth models by seismic stratigraphic architecture: the case of the Pliocene-Quaternary Fucino Basin (Central Apennines, Italy). Basin Res. 33, 2118–2156. https://doi.org/10.1111/bre.12551.
14. Improta, L., Ferranti, L., De Martini, P. M., Piscitelli, S., Bruno, P. P., Burrato, P., Maschio, L. (2010). Detecting young, slow-slipping active faults by geologic and multidisciplinary high-resolution geophysical investigations: a case study from the Apennine seismic belt, Italy. Journal of Geophysical Research, 115, B11307. https://doi.org/10.1029/2010JB000871.
15. Bello, S., de Nardis, R., Scarpa, R., Brozzetti, F., Cirillo, D., Ferrarini, F., di Lieto, B., Arrowsmith, R.J… Lavecchia, G. (2021). Fault pattern and seismotectonic style of the Campania–Lucania 1980 earthquake (Mw 6.9, Southern Italy): New multidisciplinary constraints. Frontiers in Earth Science, 8, 608063.
16. Ercoli M, Carboni F, Akimbekova A, Carbonell RB and Barchi MR (2023), Evidencing subtle faults in deep seismic reflection profiles: data pre-conditioning and seismic attribute analysis of the legacy CROP-04 profile. Front. Earth Sci. 11:1119554. doi: https://doi.org/10.3389/feart.2023.1119554

17. Ferranti, L., Carboni, F., Akimbekova, A., Ercoli, M., Bello, S., Brozzetti, F., …& Toscani, G. (2024). Structural architecture and tectonic evolution of the Campania-Lucania arc (Southern Apennines, Italy): Constraints from seismic reflection profiles, well data and structural-geologic analysis. <background-color:;i>Tectonophysics</background-color:;i>, <background-color:;i>879</background-color:;i>, 230313.

18. Improta, L., Bonagura, M., Capuano, P., Iannaccone, G., (2003). An integrated geophysical investigation of the upper crust in the epicentral area of the 1980, ms = 6.9, Irpinia earthquake (Southern Italy), Tectonophysics, 361 (1–2), 139–169.

19. Bruno, P. P., Castiello, A., & Improta, L., (2010). Ultrashallow seismic imaging of the causative fault of 1980, M6. 9, southern Italy earthquake by pre-stack depth migration of dense wide-aperture data. Geophysical Research Letters, 37 (19), L19302. doi:https://doi.org/10.1029/2010GL044721.

20. Bruno, P.P., Castiello, A., Villani, F., Improta, L., (2013). High-resolution densely Spaced wide-aperture seismic profiling as a Tool to Aid Seismic Hazard Assessment of Fault-Bounded Intramontane basins: application to Vallo Di Diano, Southern Italy. Bulletin of the Seismological Society of America, 103 (3): 1969–1980.

21. Aiello, G., Ascione, A., Barra, D., Munno, R., Petrosino, P., Russo Ermolli, E., and Villani F., (2007). Evolution of the late Quaternary San Gregorio Magno tectono-karstic basin (southern Italy) inferred from geomorphological, tephrostratigraphical and palaeoecological analyses: tectonic implications. Journal of Quaternary Science, 22, 233–45.

22. Ascione, A., Cinque, A., Improta, L., Villani, F., (2003). Late quaternary faulting within the Southern Apennines seismic belt: new data from Mt. Marzano area (Southern Italy). Quaternary International, 101–102, 27–41. https://doi.org/10.1016/S1040-6182(02)00127-1

23. Munno, R., & Petrosino, P., (2007). The late quaternary tephrostratigraphical record of the San Gregorio Magno basin (southern Italy). Journal of Quaternary Science, 22 (3), 247–266.

24. Galli, P., Giaccio, B., Messina, P., Peronace, E., Amato, V., Naso, G., Nomade, S., Pereira, A., Piscitelli, S., Bellanova, J., Billi, A., Blamart, D., Galderisi, A., Giocoli, A., Stabile, T., Thil, F., (2017). Middle to Late Pleistocene activity of the northern Matese fault system (southern Apennines, Italy), Tectonophysics, 699, 61–81, https://doi.org/10.1016/j.tecto.2017.01.007.

25. ISIDe Working Group. (2007). Italian Seismological Instrumental and Parametric Database (ISIDe) (Version 1). Istituto Nazionale di Geofisica e Vulcanologia (INGV). https://doi.org/10.13127/ISIDE

26. Rovida A., Locati M., Camassi R., Lolli B., Gasperini P., Antonucci A. (2022). Catalogo Parametrico dei Terremoti Italiani (CPTI15), versione 4.0 [Data set]. Istituto Nazionale di Geofisica e Vulcanologia (INGV). https://doi.org/10.13127/cpti/cpti15.4

27. Pondrelli, S., & Salimbeni, S. (2006). Italian CMT Dataset [Data set]. Istituto Nazionale di Geofisica e Vulcanologia (INGV). https://doi.org/10.13127/rcmt/italy

28. Montone, P., Mariucci, M.T., (2016). The new release of the Italian contemporary stress map. Geophysical Journal International, 205 (3), 1525–1531. https://doi.org/10.1093/gji/ggw100

29. Hippolyte, J.C., Angelier, J. and Roure, F.B., (1994). A major geodynamic change revealed by quaternary stress patterns in the Southern Apennines (Italy). Tectonophysics, 230 (3–4), 199–210.

30. Caiazzo, C., Ascione, A. and Cinque, A., (2006). Late tertiary–quaternary tectonics of the Southern Apennines (Italy): new evidences from the Tyrrhenian slope. Tectonophysics, 421 (1–2), 23–51.

31. Galli, P., (2024). Nearly Simultaneous Pairs and Triplets of Historical Destructive Earthquakes with Distant Epicenters in the Italian Apennines, Seismological Research Letters (2024) 95 (2A): 1057–1065. https://doi.org/10.1785/0220230135

32. Sieberg, A. (1932) Erdbebengeographie. Handbuch der Geophysik, 4, 708–744.

33. Valensise, G. and Pantosti, D., (2001). The investigation of potential earthquake sources in peninsular Italy: a review. Journal of Seismology, 5,287–306.

34. Ascione, A., Nardò, S., Mazzoli, S., (2020). The MS 6.9, 1980 Irpinia Earthquake from the basement to the surface: a review of Tectonic Geomorphology and Geophysical constraints, and New Data on Postseismic Deformation. Geosciences, 10 (12), 493; https://doi.org/10.3390/geosciences10120493.

35. Bollettinari, G., & Panizza, M. (1981). Una" Faglia Di superficie" presso san Gregorio Magno in occasione del sisma del 23-XI-1980 in Irpinia. Rendiconti Soc.Geol.Ital. Issn 0392–3037, 4/2, 135–136.

36. D'Addezio, G., Pantosti, D., and Valensise, G., (1991). Paleoearthquakes along the Irpinia fault at the Pantano Di San Gregorio Magno (southern Italy). Il Quaternario, 4, 121–136.

37. Accomando, F., Bonfante, A., Buonanno, M., Natale, J., Vitale, S., & Florio, G., (2023). The drone-borne magnetic survey as the optimal strategy for high-resolution investigations in presence of extremely rough terrains: the case study of the Taverna San Felice quarry dike. Journal of Applied Geophysics, 217, 105186.

38. Cordsen, A., Galbraith, M. and Peirce, J., (2000). Planning Land 3-D seismic surveys. Society of Exploration Geophysicists, 204. https://doi.org/10.1190/1.9781560801801.

39. Chaouch, A., Mari., J.L., (2006). 3-D Land Seismic Surveys: Definition of Geophysical Parameters. Oil & Gas Science and Technology - Rev. IFP, 61 (5), 611–630.

40. Cox, D. R., Newton, A. M. W., & Huuse, M., (2020). An introduction to seismic reflection data: acquisition, processing and interpretation. Regional Geology and Tectonics: Principles of Geologic Analysis, 571–603. doi:https://doi.org/10.1016/b978-0-444-64134-2.00020-1

41. Dondurur, D., (2018). Acquisition and Processing of Marine Seismic Data. Elsevier, 606.

42. Elboth, T., Presterud, I.V., Hermansen, D., (2010). Time-frequency seismic data de-noising. Geophys. Prospect. 58, 441–453.

43. Mousa, W.A., (2019). Advanced Digital Signal Processing of Seismic Data. Cambridge University Press, Cambridge.

44. Arya, V. K., & Holden, H. D. (1978). Deconvolution of seismic data-an overview. IEEE Transactions on Geoscience Electronics, 16(2), 95–98. https://doi.org/10.1109/TGE.1978.294570

45. Chunyan, X., Bancroft, J.C., Brown, R.J, Zhihong, C., (2003). Multiple Suppression: A Literature Review, CREWES Research Report, Consortium for Research in Elastic Wave Exploration Seismology.

46. Hileman, J. A., Embree, P., & Pflueger, J. C. (1968). Automated static corrections. Geophysical Prospecting, 16(3), 326–358. https://doi.org/10.1111/j.1365-2478.1968.tb01980.x.

47. Taner, M. T., & Koehler, F. (1969). Velocity spectra—digital computer derivation applications of velocity functions. Geophysics, 34(6), 859–881. https://doi.org/10.1190/1.1440058

48. Sheriff, R. E., & Geldart, L. P. (1995). Exploration Seismology. Cambridge university press.

49. Milsom, J. (2003). Field Geophysics, 25. John Wiley and Sons.

50. Yilmaz, Ö. (2001). Seismic data Analysis: Processing, Inversion, and Interpretation of Seismic data. Society of exploration geophysicists.

51. Griffiths, D.H., Turnbull, J. and Olayinka, A.I., (1990). Two-dimensional resistivity mapping with a computer-controlled array. First Break, 8 (4), https://doi.org/10.3997/1365-2397.1990008.

52. Telford, W.M., Geldart, L.P., Sheriff, R.E., (1990). Applied Geophysics. Cambridge University Press.

53. Sharma, P.V., (1997). Environmental and Engineering Geophysics. Cambridge University Press.

54. Naik, S.P, Gwon, O., Park, K, Bae, S.Y., Shin, H.C., Choi, J.H., Kim, Y.S., (2022). Localization and characterization of the southern Ulsan fault (UF) using geo-electrical imaging: implication for seismic hazard assessment in an urbanized area. Journal of Geodynamics, 151, 101919, https://doi.org/10.1016/j.jog.2022.101919.

55. Arjwech, R., Everett, M.E, Chaisuriya, S., Youngme, W., Rattanawannee, J., Saengchomphu, S., Thitimakorn, T., Somchat, K., 2021. Electrical resistivity tomographic detection of the hidden Thakek fault, Northeast Thailand. Near Surface Geophysics, 19 (4), 489–501. https://doi.org/10.1002/nsg.12165.

56. Rawat, G., Philip, G., Suresh, N., Medha & Yadav, R. (2019). Electrical resistivity tomography along the Himalayan Frontal Thrust in the northwestern Frontal Himalaya for active tectonics studies. Modeling Earth Systems and Environment, 5, 1563–1568: https://doi.org/10.1007/s40808-019-00604-z

57. Mojica, A., Pérez, T., Toral, J., Miranda, R., Franceschi, P., Calderón, C, Vergara, F., (2017). Shallow electrical resistivity imaging of the Limón fault, Chagres River Watershed, Panama Canal. Journal of Applied Geophysics, 138, 135–142: https://doi.org/10.1016/j.jappgeo.2017.01.010.

58. Berge, M.A., (2014). Electrical resistivity tomography investigations on a paleoseismological trenching study. Journal of Applied Geophysics, 109, 162–174. https://doi.org/10.1016/j.jappgeo.2014.07.022.

59. Zhu, T., Feng, R., Hao, J., Zhou, J., Wang, H., and Wang, S., (2009). The application of Electrical Resistivity Tomography to detecting a buried Fault: a Case Study. Journal of Environmental and Engineering Geophysics, 14 (3). https://doi.org/10.2113/JEEG14.3.145.

60. Suzuki, K., Toda, S., Kusunoki, K., Fujimitsu, Y., Mogi, T., Jomori, A., (2000). Case studies of electrical and electromagnetic methods applied to mapping active faults beneath the thick quaternary. Developments in Geotechnical Engineering, 84, 29–45: https://doi.org/10.1016/S0165-1250(00)80005-X.

61. Keller, G. V., Frischknecht, F.C., (1966). Dipole method for deep resistivity studies. Geophysics, 31(6), 1088–1104.

62. Loke M.H. and R.D. Barker, (1996). Rapid least-squares Inversion of Apparent Resistivity pseudosections using a Quasi-newton Method. Geophysical Prospecting 44 (1), 131–152, DOI: https://doi.org/10.1111/j.1365-2478.1996.tb00142.x

63. Reynolds J.M. (2011). An Introduction to Applied and Environmental Geophysics. Wiley-Blackwell, 712 pp.

64. Mazzini, A., Carrier, A., Sciarra, A., Fischanger, F., Winarto-Putro, A., & Lupi, M., (2021). 3D deep electrical resistivity tomography of the Lusi eruption site in East Java. Geophysical Research Letters, 48(18), e2021GL092632.

65. Lajaunie, M., Gance, J., Nevers, P., Malet, J. P., Bertrand, C., Garin, T., & Ferhat, G., (2019). Structure of the Séchilienne unstable slope from large-scale three-dimensional electrical tomography using a Resistivity distributed Automated System (R-DAS). Geophysical Journal International, 219(1), 129–147. https://doi.org/10.1093/gji/ggz259.

66. Carrier, A., Fischanger, F., Gance, J., Cocchiararo, G., Morelli, G., & Lupi, M., (2019). Deep electrical resistivity tomography for the prospection of low- to medium-enthalpy geothermal resources. Geophysical Journal International, 219 (3), 2056–2072. https://doi.org/10.1093/gji/ggz411

67. Sapia, V., Villani, F., Fischanger, F., Lupi, M., Baccheschi, P., Pantosti, D., Pucci, S., Civico, R., Sciarra, A., Smedile, A., Romano, V., De Martini, P.M., Murgia, F., Materni, V., Giannattasio, F., Pizzimenti, L., Ricci, T., Brunori, C.A., Coco, I., Improta, L., (2021). 3-D deep electrical resistivity tomography of the major basin related to the 2016 mw 6.5 central Italy earthquake fault. Tectonics, 40 (4), e2020TC006628.

68. Barker, R. D. (1989). Depth of investigation of collinear symmetrical four-electrode arrays. Geophysics, 54 (8), 1031–1037. https://doi.org/10.1190/1.1442728

69. Blakely, R.J., (1996). Potential Theory in Gravity and Magnetic Applications, Cambridge University Press.

70. Kelemework, Y., Milano, M., La Manna, M., De Alteriis, G., Iorio, M. & Fedi, M., (2021). Crustal structure in the Campanian region (Southern Apennines, Italy) from potential field modelling. Scientific Reports 11, 14510. https://doi.org/10.1038/s41598-021-93945-8.

71. Tarquini, S., Isola, I., Favalli, M., Battistini, A., & Dotta, G. T., (2023). A Digital Elevation Model of Italy with a 10 Meters cell size (Version 1.1). Istituto Nazionale di Geofisica e Vulcanologia (INGV): Roma, Italy, 1, 1–2.

72. & Alsdorf, D., (2007). The shuttle radar topography mission. Reviews of geophysics,45 (2).

73. Totaro, F., Insinga, D. D., Lirer, F., Margaritelli, G., i Caparrós, A. C., de la Fuente, M., & Petrosino, P., (2022). The late pleistocene to Holocene tephra record of ND14Q site (southern Adriatic Sea): traceability and preservation of Neapolitan explosive products in the marine realm. Journal of Volcanology and Geothermal Research, 423, 107461. https://doi.org/10.1016/j.jvolgeores.2021.107461

74. Crocitti, M., Sulpizio, R., Insinga, D. D., De Rosa, R., Donato, P., Iorio, M., Zanchetta, G., Barca, D., & Lubritto, C., (2019). On ash dispersal from moderately explosive volcanic eruptions: examples from Holocene and late pleistocene eruptions of Italian volcanoes. Journal of Volcanology and Geothermal Research, 385, 198–221.

75. Accomando, F., Vitale, A., Bonfante, A., Buonanno, M., & Florio, G., (2021). Performance of two different flight configurations for drone-borne magnetic data. Sensors, 21(17), 5736.

76. Mellett, J.S., (1995). Ground penetrating radar applications in engineering, environmental management, and geology. Journal of Applied Geophysics, 33 (1–3), 157–166, ISSN 0926-9851, https://doi.org/10.1016/0926-9851(95)90038-1.

77. Noviello, C.; Gennarelli, G.; Esposito, G.; Ludeno, G.; Fasano, G.; Capozzoli, L.; Soldovieri, F.; Catapano, I., (2022). An overview on down-looking UAV-Based GPR systems. Remote Sens., 14, 3245. https://doi.org/10.3390/rs14143245

78. Massaro, N. Savino, S. Selicato, A. Panarese, A. Galiano and Dipierro, G., (2021). Thermal IR and GPR UAV and Vehicle Embedded Sensor Non-Invasive Systems for Road and Bridge Inspections. IEEE International Workshop on Metrology for Industry 4.0 & IoT (MetroInd4.0&IoT), Rome, Italy, 248–253, https://doi.org/10.1109/MetroInd4.0IoT51437.2021.9488483.

79. Lijcklama à Nijeholt, L.; Kronshorst, T.Y.; Teeffelen, K.v.; van Manen, B.; Emaus, R.; Knotter, J.; Mersha, A. Utilizing drone-based ground-penetrating radar for crime investigations in localizing and identifying Clandestine Graves. Sensors 2023, 23, 7119. https://doi.org/10.3390/s23167119

80. Blindow, N., Eisenburger, D., Illich, B., Petzold, H., Richter, T., (2007). Ground Penetrating Radar. In: Environmental Geology. Springer, Berlin, Heidelberg. https://doi.org/10.1007/978-3-540-74671-3_10

81. Valence, E., Baraer, M., Rosa, E., Barbecot, F., and Monty, C., (2022). Drone-based ground-penetrating radar (GPR) application to snow hydrology. The Cryosphere, 16, 3843–3860. https://doi.org/10.5194/tc-16-3843.

82. Filkin, T.; Lipin, I.; Sliusar, N., (2023). Integrating a UAV System based on Pixhawk with a laser methane Mini detector to study methane emissions. Drones, 7, 625. https://doi.org/10.3390/drones7100625.

83. Ruols B, Baron L, Irving J., (2023). Development of a drone-based ground-penetrating radar system for efficient and safe 3D and 4D surveying of alpine glaciers. Journal of Glaciology. 1–12. https://doi.org/10.1017/jog.2023.83.

84. Jol, H. M. (2009). Ground Penetrating Radar: Theory and Applications. Elsevier.

85. Daniels, D. J. (2004). Ground Penetrating Radar (2nd ed.). The Institution of Engineering and Technology.

86. Annan, A. P. (2005). Ground-Penetrating Radar. In D. K. Butler (Ed.), Near-Surface Geophysics (pp. 357–438). Society of Exploration Geophysicists.

87. Salimon, C. I., Davidson, E. A., Victoria, R. L., Melo, A. W. F., (2004). CO2 flux from soil in pastures and forests in southwestern Amazonia. Global Change Biology, 10 (5), 833–843.

88. Troiano, A., Di Giuseppe, M. G., Petrillo, Z., & Patella, D. (2009). Imaging 2D structures by the CSAMT method: application to the Pantano Di S. Gregorio Magno faulted basin (Southern Italy). Journal of Geophysics and Engineering, 6(2), 120–130.

89. Florio, G., (2020). The estimation of depth to basement under sedimentary basins from gravity data: review of approaches and the ITRESC Method, with an application to the Yucca Flat Basin (Nevada). Springer Link, 41, 935–961.

90. Florio, G., Fed, M., Cella, F., (2023). A fractional vertical derivative technique for regional-residual separation. Geophysical Journal International, 232 (1), 601–614, https://doi.org/10.1093/gji/ggac348.

91. Galli, P.A.C., Giocoli, A., Peronace, E. et al. Integrated near surface geophysics across the active Mount Marzano Fault System (southern Italy): seismogenic hints. Int J Earth Sci (Geol Rundsch) 103, 315–325 (2014). https://doi.org/10.1007/s00531-013-0944-y

92. Raich, J.W., and Schlesinger, W.H., 1992. The global carbon dioxide flux in soil respiration and its relationship to vegetation and climate. Tellus B (44), 81–99. https://doi.org/10.1034/j.1600-0889.1992.t01-1-00001.x7

93. Vitale, S., Albanese, S., Di Maio, R., Ambrosino, M., Cicchella, D., De Paola, C., Fabozzi, C., Notaro, P., Pagliara, F., Prinzi, E.P., Salone, R., Ciarcia, S., (2023). Insights on the active Southern Matese Fault system through geological, geochemical, and geophysical investigations of the CO_2 gas vent in the Solopaca area (southern Apennines, Italy). Tectonophysics, 846, 229657. https://doi.org/10.1016/j.tecto.2022.229657.

94. Taussi, M., Brogi, A., Liotta, D., Nisi, B., Perrini, M., Vaselli, O., … & Zucchi, M. (2022). CO2 and heat energy transport by enhanced fracture permeability in the Monterotondo Marittimo-Sasso Pisano transfer fault system (Larderello Geothermal Field, Italy). <background-color:;i>Geothermics</background-color:;i>, <background-color:;i>105</background-color:;i>, 102531.

95. Ciotoli, G., Bigi, S., Tartarello, C., Sacco, P., Lombardi, S., Ascione, A. and Mazzoli, S., 2014. Soil gas distribution in the main coseismic surface rupture zone of the 1980, ms = 6.9, Irpinia earthquake (southern Italy). Journal of Geophysical Research: Solid Earth, 119(3), pp.2440–2461.

96. Ascione, A., Iannace, A., Imbriale, P., Santangelo, N., Santo, A., (2014). Tufa and travertines of southern Italy: deep-seated, fault-related CO2 as the key control in precipitation. Terra Nova, 26 (1), 1–13. https://doi.org/10.1111/ter.12059

97. Feriozzi, F., Improta, L., Maesano, F. E., De Gori, P., & Basili, R. (2024). The 3D crustal structure in the epicentral region of the 1980, Mw 6.9, Southern Apennines earthquake (southern Italy): new constraints from the integration of seismic exploration data, deep wells, and local earthquake tomography. Tectonics, 43, https://doi.org/10.1029/2023TC008056.

Acknowledgements

Author contributions

The project team, and all phases of field data acquisition, analysis, and interpretation, were supervised by P.P.G. Bruno, with assistance from G. Ferrara. P.P.G. Bruno planned the acquisition of 2D and 3D seismic data, supported by G. Ferrara and S. Maraio. Seismic data were acquired by P.P.G. Bruno, S. Maraio, L. Improta, P.M. De Martini and D. Iacopini. Processing and interpretation of the seismic data were led by P.P.G. Bruno and G. Ferrara, with input on interpretation from L. Improta and D. Iacopini. ERT data were acquired by V. Di Fiore, D. Tarallo, M. Punzo, G. Ferrara, V. Paoletti, and G. Cavuoto, and processed by V. Di Fiore, D. Tarallo, and M. Punzo. M. Zambrano and T. Volatili supervised the acquisition and processing of FullWaver data. Gravity data were acquired and processed by G. Florio, M. Milano, V. Paoletti, F. Muccini, G. Ferrara, and S. Maraio. Magnetic data acquisition and processing were conducted by G. Florio and F. Accomando. GPR data were acquired and processed by N.A. Famiglietti and A. Memmolo. Drone acquisition was supervised and planned by A.M. Vicari. S. Albanese, A. Iannone, and L.R. Pacifico acquired and processed CO_2 flux data. The manuscript was primarily authored by P.P.G. Bruno, with support from G. Ferrara and L. Improta. Specific contributions to paragraphs were made by G. Florio, F. Accomando, M. Milano, M. Zambrano, F. Accomando, and L. Improta. Finalization of the manuscript involved input from all authors.

Declarations

Competing interests

The co-author M. Milano is member of the Editorial Board of Scientific Reports and has no competing interest. The other authors, P.P.G. Bruno, G. Ferrara, M. Zambrano, S. Maraio, L. Improta, T. Volatili, V. Di Fiore, G. Florio, S. Albanese, D. Iacopini, F. Accomando, D. Tarallo, P.M. De Martini, F. Muccini, M. Punzo, V. Paoletti, A. Iannone, L.R. Pacifico, A. Vicari, N.A. Famiglietti, A. Memmolo, G. Cavuoto, have no competing interest. Supplementary Information accompanies this paper. Reprints and permission information is available online at: http://npg.nature.com/reprintsandpermissions/.(giuseppe.ferrara@unina.it).

Additional information

Supplementary Information The online version contains supplementary material available at https://doi.org/10.1038/s41598-024-75276-6.

Correspondence and requests for materials should be addressed to G.F.

Reprints and permissions information is available at www.nature.com/reprints.

Publisher's note Springer Nature remains neutral with regard to jurisdictional claims in published maps and institutional affiliations.